Naval Research Laboratory

Washington, DC 20375-5320

NRL/MR/6180--15-9601

Lithium Battery Safety/Cell-to-Cell Failure Project FY14 Progress Report

Neil S. Spinner

National Research Council Postdoctoral Associate
Navy Technology Center for Safety and Survivability
Chemistry Division

Ramagopal Ananth
Steven G. Tuttle
Susan L. Rose-Pehrsson

Navy Technology Center for Safety and Survivability
Chemistry Division

Ryan Mazurick

Naval Research Enterprise Internship Program
Navy Technology Center for Safety and Survivability
Chemistry Division

Andrew Brandon

Pathways Internship Program
Navy Technology Center for Safety and Survivability
Chemistry Division

March 6, 2015

Approved for public release; distribution is unlimited.

REPORT DOCUMENTATION PAGE

Form Approved
OMB No. 0704-0188

Public reporting burden for this collection of information is estimated to average 1 hour per response, including the time for reviewing instructions, searching existing data sources, gathering and maintaining the data needed, and completing and reviewing this collection of information. Send comments regarding this burden estimate or any other aspect of this collection of information, including suggestions for reducing this burden to Department of Defense, Washington Headquarters Services, Directorate for Information Operations and Reports (0704-0188), 1215 Jefferson Davis Highway, Suite 1204, Arlington, VA 22202-4302. Respondents should be aware that notwithstanding any other provision of law, no person shall be subject to any penalty for failing to comply with a collection of information if it does not display a currently valid OMB control number. **PLEASE DO NOT RETURN YOUR FORM TO THE ABOVE ADDRESS.**

1. REPORT DATE *(DD-MM-YYYY)*	2. REPORT TYPE	3. DATES COVERED *(From - To)*
06-03-2015	Memorandum Report	January 2014 – September 2014

4. TITLE AND SUBTITLE

Lithium Battery Safety/Cell-to-Cell Failure Project FY14 Progress Report

5a. CONTRACT NUMBER
N0001414WXZ0004

5b. GRANT NUMBER

5c. PROGRAM ELEMENT NUMBER
0602123N

6. AUTHOR(S)

Neil S. Spinner,* Ramagopal Ananth, Steven G. Tuttle, Susan L. Rose-Pehrsson, Ryan Mazurick,† and Andrew Brandon‡

5d. PROJECT NUMBER

5e. TASK NUMBER

5f. WORK UNIT NUMBER
61-9496-A2-5

7. PERFORMING ORGANIZATION NAME(S) AND ADDRESS(ES)

Naval Research Laboratory
4555 Overlook Avenue, SW
Washington, DC 20375-5320

8. PERFORMING ORGANIZATION REPORT NUMBER

NRL/MR/6180--15-9601

9. SPONSORING / MONITORING AGENCY NAME(S) AND ADDRESS(ES)

Office of Naval Research
One Liberty Center
875 N. Randolph St., Suite 1425
Arlington, Virginia 22203-1995

10. SPONSOR / MONITOR'S ACRONYM(S)

ONR

11. SPONSOR / MONITOR'S REPORT NUMBER(S)

12. DISTRIBUTION / AVAILABILITY STATEMENT

Approved for public release; distribution is unlimited.

13. SUPPLEMENTARY NOTES

*National Research Council Postdoctoral Associate
†Naval Research Enterprise Internship Program
‡Pathways Internship Program

14. ABSTRACT

The Navy Technology Center for Safety and Survivability of the Naval Research Laboratory is investigating lithium-ion battery cell-to-cell failure modes through development of predictive modeling capabilities and experimental measurements. Recent progress in this project has included determination of critical thermophysical properties of commercial 18650 lithium-ion batteries, such as thermal conductivity, heat capacity and density, non-invasive internal temperature monitoring using electrochemical impedance spectroscopy (EIS), novel surrogate cell design mimicking real battery anisotropic thermal properties, and thermal modeling up to the point of cell failure. Model predictions compared well with experimental data, and this report demonstrates significant progress towards understanding and predicting cell-to-cell failure.

15. SUBJECT TERMS

Hexamethylene triperoxidediamine
Explosive vapor
Explosive detection
Headspace analysis

16. SECURITY CLASSIFICATION OF:			17. LIMITATION OF ABSTRACT	18. NUMBER OF PAGES	19a. NAME OF RESPONSIBLE PERSON
a. REPORT	b. ABSTRACT	c. THIS PAGE			Susan L. Rose-Pehrsson
Unclassified Unlimited	Unclassified Unlimited	Unclassified Unlimited	Unclassified Unlimited	47	19b. TELEPHONE NUMBER *(include area code)* (202) 767-3138

Contents

1.0 Background and Motivation 1
2.0 Technical Capabilities/Improvements 2
3.0 Progress 3
3.1 Surrogate Cell Design 3
3.2 Lithium-ion Battery Thermal Properties 7
3.3 EIS-based Non-Invasive Internal Temperature Determination 17
3.4 Multi-Cell Model Development and Analysis 26
4.0 Summary & Conclusions 37
5.0 References 39

1.0 Background and Motivation

The safe use of lithium-ion batteries requires an understanding of battery failure modes, how to avoid failure scenarios, how to prepare for possible failure scenarios, and how to mitigate failure consequences. Battery failure begins at the cell level, and therefore it is crucial to increase our understanding of how individual cell components and properties influence these potentially catastrophic failure events. However, the majority of effort until recently has been focused on cell and battery development, not safety. Researchers and cell developers have previously, and are currently, measuring and modeling electrode characteristics and investigating optimum electrolyte properties and cell configurations. The rapid implementation of lithium-ion battery power sources has resulted in an abrupt call to understand lithium-ion battery safety following several recent and high profile energetic failure events [1-4].

While lithium-ion battery failure begins at the cell level, it is also critical to investigate the dynamics of large format battery packs that are commonly used in Navy applications such as missiles, torpedoes, UUVs, mines, submarines, sonobuoys, field communications, and night vision [5-8]. Assuring safe use of lithium-ion batteries will require protecting against the full range of impacts and consequences on neighboring cells in a large format battery pack as one cell undergoes failure. While models do exist for commercial and Department of Energy (DOE) applications, such as automotive batteries [9-12], their use of experimental data to capture the impact on nearby cells of high temperatures, gas venting, fire, and shrapnel due to cell failure as related to Navy and shipboard applications has been limited. A predictive capability is needed to accurately determine a maximum credible event (MCE) for battery behavior and to extrapolate cell behavior to full scale battery systems used on Navy platforms, which will ultimately reduce cost in testing and certification.

Higher-level models that predict different aspects of platform impact, e.g. fire spread [13,14] and structural damage [15], will need modifications (i.e. additional modules) to describe and predict the consequences of catastrophic battery failure effects. These required modifications should be possible with upgrades that enable a more accurate description of battery casualty and can be directly fed into models. Conversely, lower-level thermo-electrochemical models and studies exist for describing the internal condition inside a single cell [16-19]. These models describing the internal chemistry and micro-structure of individual cells have provided valuable insights into the sources of cell failure, but fail to extend to multiple cells. Thus, there is a knowledge gap between single cell and large format lithium-ion battery failure.

Detailed testing to measure the impact of a single cell failure on nearby cells has been limited [20-24]. Because there are several different ways in which the failure of a single cell may spread to neighboring cells, a number of parameters must be measured to adequately document what conditions cause failure to spread. Thus, through this program we have been developing the necessary scientific and experimental infrastructure to investigate cell-to-cell failure propagation in lithium-ion batteries and provide robust experimental data for computational models.

Manuscript approved November 21, 2014.

Collection of these experimental data for the development and verification of new computational models needs to be carried out across multiple domain scales. First, fundamental aspects of individual lithium-ion battery cell chemistry and safety mechanisms before, during, and after failure must be elucidated via electrochemical testing, measurements of energy and mass transfer from induced failure events, and determination of thermophysical properties. Second, battery packs containing numerous 18650-type active and surrogate cells need to be constructed to investigate cell-to-cell propagation of failure events. Surrogate cells must be designed and constructed to closely mimic the anisotropic thermal properties of real 18650 lithium-ion batteries without any active or flammable materials. The use of surrogate cells is beneficial in that it eliminates the need to use large numbers of active cells in each test, thereby reducing cost and improving safety, and also allows real-time measurement of the internal temperature at multiple locations inside a cell during testing. With these data, computational models can be developed and experimentally verified to enable prediction of the thermal and electrochemical behavior of lithium-ion batteries leading up to, during, and immediately after a failure event.

2.0 Technical Capabilities/Improvements

The NRL Chesapeake Bay Detachment (NRL-CBD) facility located in Chesapeake Beach, Maryland houses a 5-m^3 (177 ft^3) two-man decompression chamber that has been re-purposed as an environmental test chamber. Figure 1 shows an image of the chamber and a diagram of the locations of various ports and instrumentation. In the past four to five years, the 5-m^3 chamber has been used by the Navy Technology Center for Safety and Survivability, Code 6180, primarily to investigate lithium-ion battery safety, specifically identifying the chemical species released during a single cell failure event [25].

Numerous upgrades and improvements have been instituted over the past few years to conduct these experiments, including implementation of various equipment and instrumentation such as high speed visible and infrared (IR) cameras, compact reconfigurable input/output devices

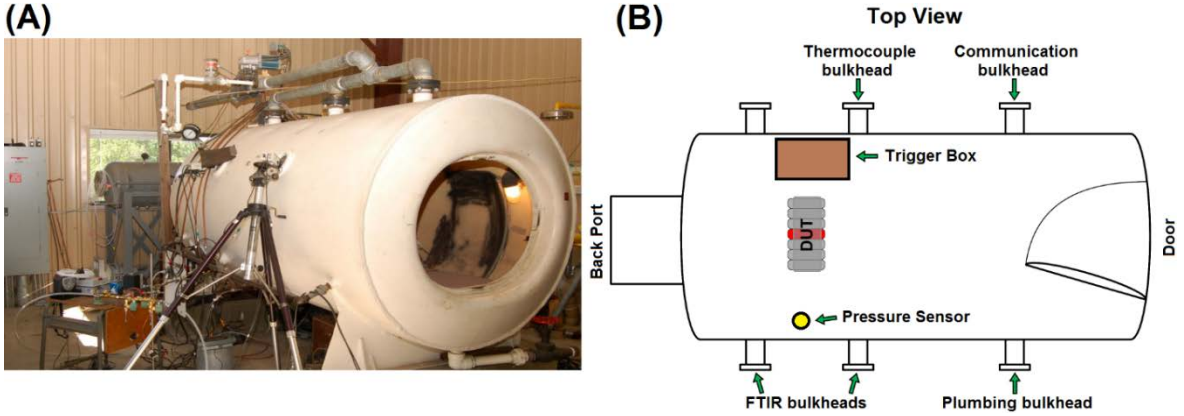

Figure 1. (A) Photograph of the 5-m^3 (177 ft^3) two-man decompression chamber that has been re-purposed into an environmental test chamber at NRL-CBD. (B) Diagram showing the top view of the chamber with relative locations of external ports and selected equipment including the trigger box, pressure sensor, and device under test (DUT).

(cRIOs), real-time gas analyzers, a Fourier transform infrared spectrometer (FTIR), heat flux gauges, thermocouples, and surrogate cells. We recently published a Memorandum Report that details the up-to-date modifications and capabilities of the test chamber, along with results and in-depth analysis of single and mutli-cell 18650 lithium-ion battery failure tests [26]. We will continue to build upon the progress discussed in this recent publication, making further modifications and upgrades to the environmental test chamber as needed.

The Navy Technology Center for Safety and Survivability has a range of computational modeling tools to examine the thermal, chemical, and electrical behavior of a range of scientific and engineering systems. Relevant to this program, internal software capability includes COMSOL, a finite element modeling tool, and ANSYS/FLUENT, a multi-physics finite volume modeling tool, both of which are widely used for coupled fluid flow, chemistry, electrical, thermal, and mechanical simulations. In the last two years, we have used internal division funding to construct a high performance computational cluster for running ANSYS/FLUENT. The hardware, software, and network capability has matured to where it is accessible and operational for this and a range of large modeling problems.

3.0 Progress

3.1 Surrogate Cell Design

The initial design for surrogate cells used in previous tests [26] consisted of an aluminum core with grooves for inserted thermocouples in three locations, and a diagram of this surrogate cell iteration is shown in Figure 2. Aluminum was originally selected as the surrogate cell core material due to its similar thermal properties to those of an active cell, and Table 1 lists reported values for the heat capacity (C_p), density (ρ), and thermal conductivity (k) of several materials, including aluminum and typical commercial 18650 lithium-ion batteries. As can be seen in Table 1, aluminum was a good initial choice due to its analogous heat capacity and density values. However, it was clear from our data, and via comparison of values, that there was a severe

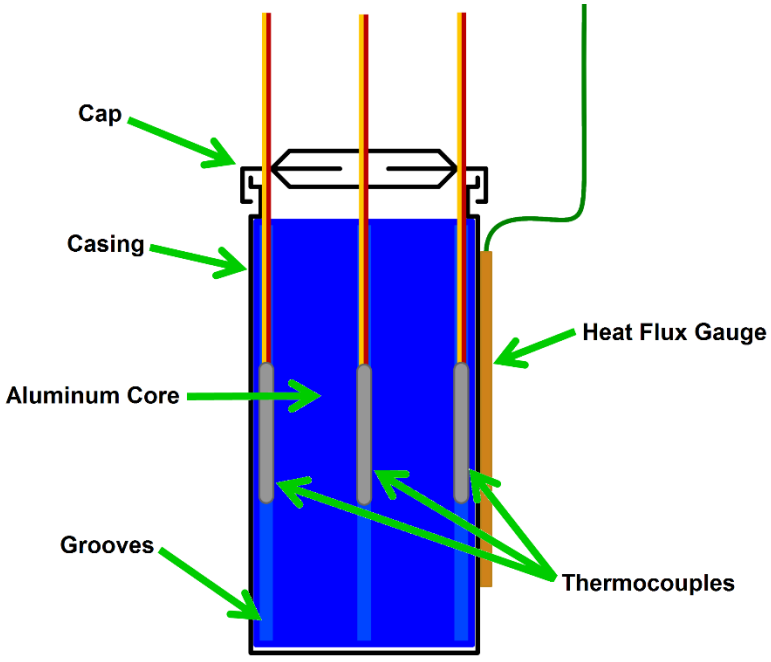

Figure 2. Original design of 18650-type surrogate cell consisting of aluminum core used in results from our previously published work [26].

mismatch in thermal conductivities. Analysis of different thermocouple positions within a single surrogate cell revealed no temperature variation due to the large thermal conductivity of the aluminum core. This behavior is not representative of a real cell, where its low radial thermal conductivity produces a temperature gradient from the outside to the center of the rolled electrode components (termed the "jelly roll") of around 5-15°C, with even higher values possible during either rapid charging/discharging or strong convective heating/cooling [27,28]. In addition, real 18650 batteries exhibit a degree of anisotropy (as illustrated in Table 1 which lists values for radial vs. axial thermal conductivities, showing one to two orders of magnitude difference) as a result of the geometry of the jelly roll that cannot be adequately mimicked using a solid cylinder of aluminum. Therefore, it became apparent that a new surrogate cell design was necessary to more accurately capture the real thermal properties and behavior of commercial cells.

Table 1. Values for heat capacity (C_p), density (ρ), and thermal conductivity (k) of aluminum (type 6061) and typical 18650 commercial lithium-ion batteries. Sources: a – [18]; b – [27]; c – [29]; d – [30]; e – [31]; f – [32]; g – [33]; h – [34]; i – [35]; k – [36]; m – [37]; n – [38]; p – manufacturer material specifications; r – in-house experimentally determined value.

	Aluminum	Stainless Steel	Mica	Typical Commercial 18650 Li-ion Cell
C_p (J/kg-K)	860-890[c,d,r]	500[p]	800-820[f,g]	800-1700[a,b,i,k,m,r]
ρ (kg/m^3)	2700[c]	8030[p]	2900[c,f]	2300-3000[b,k,r]
k (W/m-K)	154-205[d,e]	16.2[p]	0.45 (radial)[c,h] 4 (axial)[h]	0.2-0.6 (radial)[a,b,i,k,n] 30 (axial)[a,b,i,n]

A jelly roll surrogate cell design was fabricated using alternating layers of non-conductive mica and stainless steel shim, mimicking the construction of a real cell which consists of layers of aluminum and copper foil current collectors separated by a non-conductive polymer separator (typically polypropylene and/or polyethylene). Figure 3 shows a diagram of this new surrogate cell design, which also contained a center thermocouple that was affixed to the inside layer just prior to rolling, and two thermocouples on either side of the outside layer after rolling, but still contained inside the cell casing. In this way, the new surrogate cells were similar to the old with respect to thermocouple placement so that consistency can be maintained with previous work during future analysis of heat propagation.

Using a microclimate benchtop temperature test chamber (Cincinnati Sub-Zero) along with a cRIO (as described in detail in [26]) for temperature monitoring of both internal and externally-attached thermocouples, new surrogate cells were tested to observe their thermal response to temperature change. For comparison, the jelly roll from an active cell (Tenergy $LiCoO_2$ 18650,

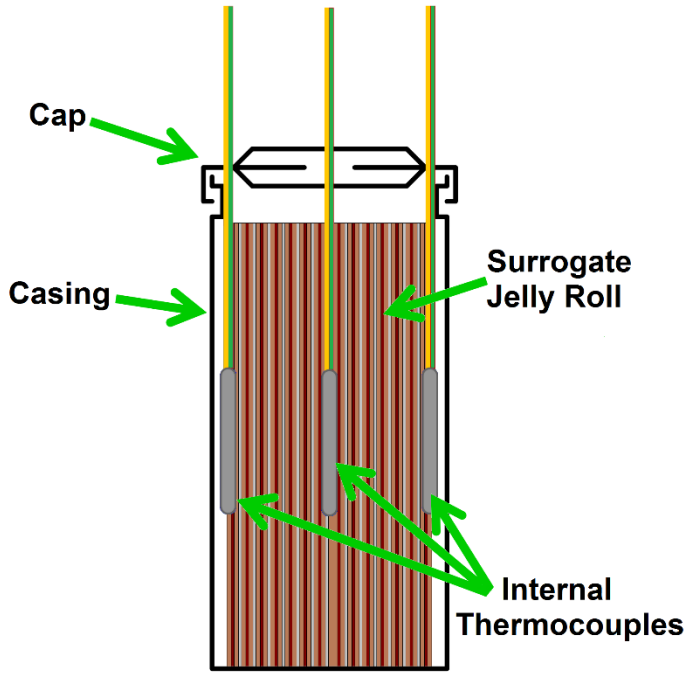

Figure 3. New surrogate cell design with jelly roll-style for internal components. Three internal thermocouples affixed to obtain radial temperature distribution and to maintain consistency with previous aluminum-core design. Jelly roll composed of alternating layers of mica and stainless steel sheets.

2600 mAh battery) was cut out of its cell casing (in a fully discharged state for safety), trimmed, and instrumented with three thermocouples in similar fashion to the surrogate cell. The components were then inserted into a new casing, crimped, and sealed. This cell with real components was termed a "dead" cell for all experiments. In addition, an unmodified active cell was instrumented with three external thermocouples and used for comparison as well. The three 18650 cells ("surrogate", "dead", and "active") were subjected to three step changes in temperature lasting two hours each (in order: 0°C, 50°C, then 20°C). In particular, thermal behavior during heat up and cool down to each temperature set point was analyzed.

Surface temperature measurements for all three cells during this step change experiment are shown in Figure 4. All three cells showed similar responses, and the temperature set point was reached within 1-2°C after around 18-20 minutes for the smaller temperature changes (room temperature to 0°C, 50°C to 20°C). For the larger change (0°C to 50°C), predictably, the response was slightly slower, taking around 29-30 minutes for all cells to reach the set point. Some of this delay can be attributed to the test chamber itself which contained some inherent lag during the temperature change, introducing some uncertainty during the transient heating/cooling periods until the chamber was able to reach steady conditions. Interestingly, during these transient periods, the maximum instantaneous temperature difference at any time between the active cell and surrogate cell was lower (around 5-6°C) than that of the active and dead cells (around 6-9°C). This was a curious result since it was expected that the dead cell's thermal behavior would be most similar to that of the active cell. However, during the preparation of the dead cell it is likely that the electrolyte dried out considerably as the components were exposed to ambient conditions for an extended period of time. In addition, the jelly roll needed to be trimmed so that it would fit inside the new cell casing once thermocouples were attached to either side. Due to these necessary modifications, the dead cell was compositionally different from the active cell despite having the same jelly roll materials, and these differences likely contributed to the contrast in thermal behavior. On the other hand, the

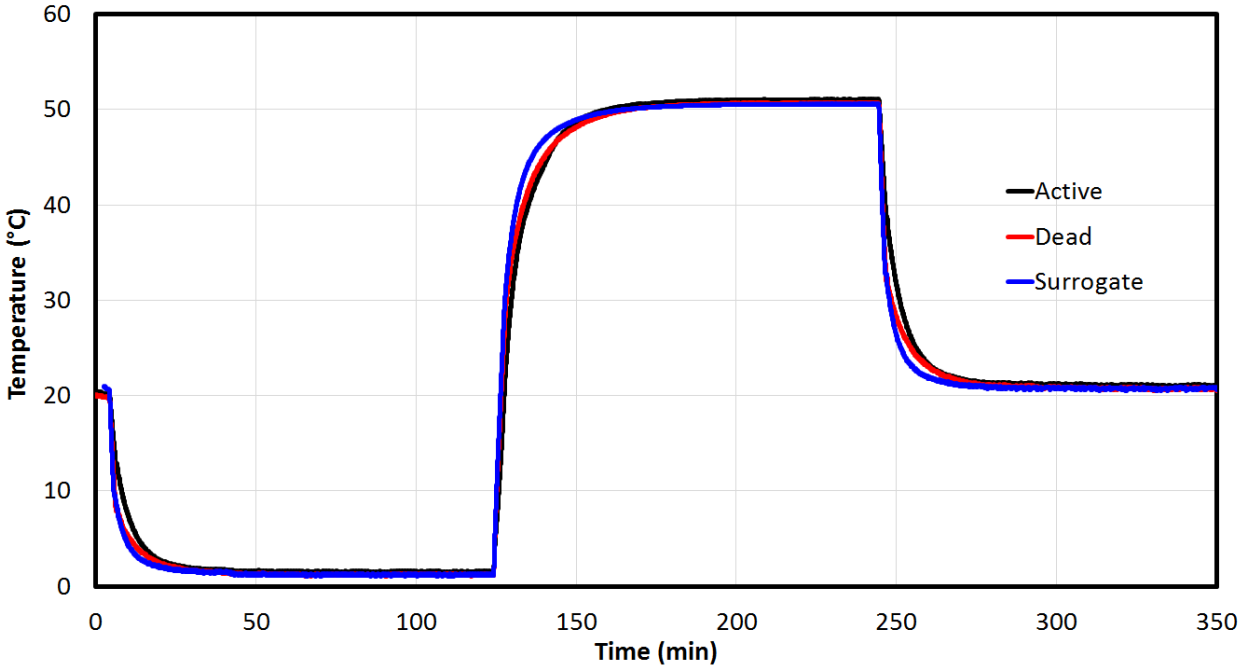

Figure 4. Thermal response of active, dead, and surrogate cells inside a microclimate benchtop temperature test chamber. The chamber was programmed to go to three consecutive set points (0°C, 50°C, 20°C) with a dwell at each temperature for two hours. Temperatures measured via thermocouples attached to the surface of each cell.

lower temperature difference between active and surrogate cells highlights the promising ability of this new surrogate cell to closely mimic the thermal response and properties of an active cell.

Figure 5 shows the radial temperature distribution inside the surrogate cell during the temperature change between 0°C and 50°C. The maximum difference in temperatures between the outside and center thermocouples at any time was around 6.5°C, which is consistent with values found in the literature for radial temperature differences in real batteries [27,28]. This result, along with the overall thermal response observed in Figure 4, illustrates how this new jelly roll surrogate cell design is effective in mimicking the properties and behavior of a real, active 18650 battery without the use of any flammable or hazardous materials. Multiple surrogate cells with this design will be produced and used to observe temperature changes and heat propagation in large format battery packs during cell-to-cell failure events. The unique jelly roll design will also enable varying package configurations, including horizontal and vertical stacking of cells, to observe both radial and axial heat flux while taking advantage of the anisotropic thermal properties consistent with real 18650 batteries. Data from these multi-cell failure tests will be combined with the results shown in this report, and the final manuscript will be submitted for publication in a high impact scientific journal [39].

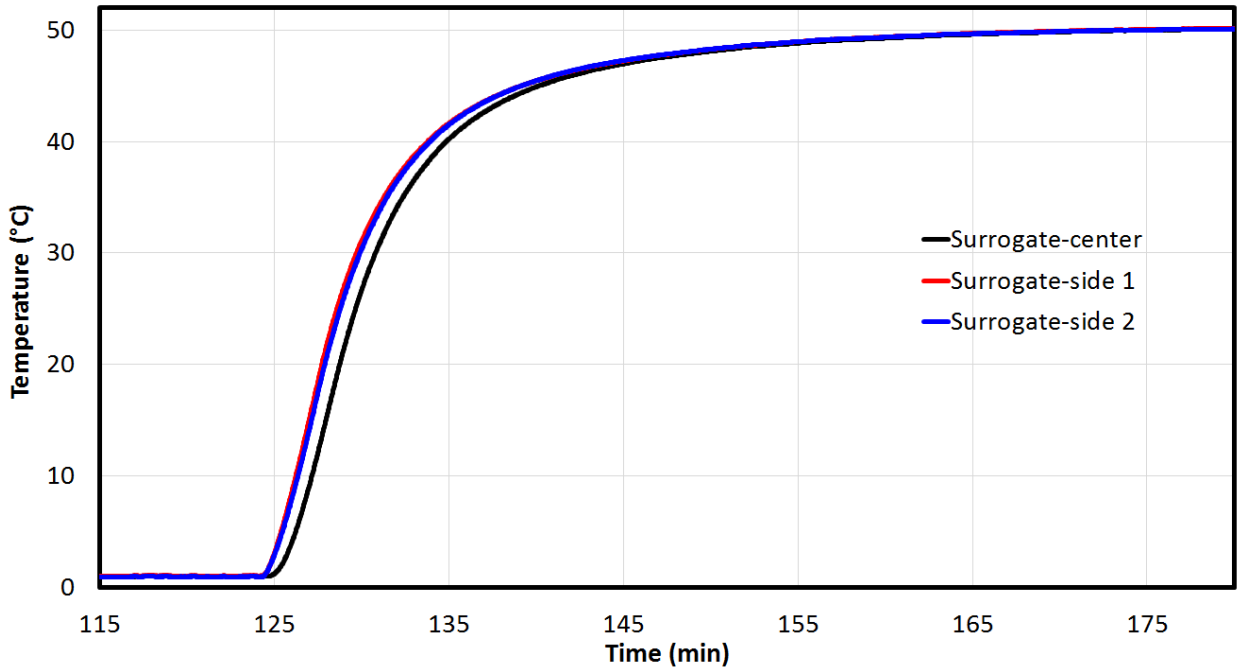

Figure 5. Radial temperature distribution inside surrogate cell during step change from 0°C to 50°C. Temperatures monitored from three internal thermocouples (see Figure 3 for diagram) to observe difference between center and side positions during heating event.

3.2 Lithium-ion Battery Thermal Properties

Determining thermophysical properties such as heat capacity, density, and thermal conductivity of lithium-ion batteries is of great importance for the development of predictive models. These properties were elucidated for commercial 18650 lithium-ion batteries using various calorimetric, numerical, and analytical techniques. Methods were also verified using materials of known thermophysical properties, and values were cross-checked with those found in literature to determine accuracy.

There are two principle reasons thermal properties cannot be calculated from the properties and masses of the individual components. First, manufacturers are unwilling to provide detailed component and material descriptions of the batteries they sell in order to protect their competitive market share and intellectual property. More importantly, the thermal properties of the cell is dependent on the assembly process. The layers of different materials not only have inherent thermal properties, but the nature of their contact, porosity, and geometry determine how heat is transferred within a cell. Therefore, a mass-averaged calculation of the components would not provide accurate heat capacity or thermal conductivity.

The first technique that was performed was convective heat transfer with an analytical analysis. Using previous temperature vs. time experiments for active batteries from the new surrogate cell

design tests with the microclimate benchtop temperature test chamber, an analytical solution to the multi-dimensional radial heat equation, Equation 1, was determined and the data was fit to obtain approximations for k and C_p.

$$\frac{\rho C_p}{k}\frac{\partial T}{\partial t} = \frac{1}{r}\frac{\partial}{\partial r}\left(r\frac{\partial T}{\partial r}\right) \tag{1}$$

In Equation 1, T is the temperature, t is the time, and r is the radial position. The experimental setup consisted of the cylindrical battery (Tenergy $LiCoO_2$) inside the chamber at an initial temperature, T_o, followed by a step change to the final chamber temperature, T_∞. Assuming that the air within the chamber reached T_∞ quickly, the battery heated/cooled from T_o to T_∞ via convective heat transfer at the surface (either to or from the battery from/to the chamber environment, depending on the direction of the step change) propagating radially via thermal conduction. The boundary and initial conditions are therefore written as:

$$\left.\frac{\partial T}{\partial r}\right|_{r=0} = 0 \tag{2}$$

$$-k\left.\frac{\partial T}{\partial r}\right|_{r=R} = h(T|_{r=R} - T_\infty) \tag{3}$$

$$T|_{t=0} = T_o \text{ (for all r)} \tag{4}$$

where h is the convective heat transfer coefficient and R is the radius of the battery (9 mm). The analytical solution to Equation 1 with boundary and initial conditions shown in Equations 2-4 is

$$T(r,t) = T_\infty + \frac{2(T_o - T_\infty)}{R}\sum_{n=1}^{\infty}\frac{1}{\lambda_n}\frac{J_1(\lambda_n R)J_0(\lambda_n r)}{J_0^2(\lambda_n R)+J_1^2(\lambda_n R)}e^{-\alpha\lambda_n^2 t} \tag{5}$$

where J_0 and J_1 are Bessel functions of the first kind of orders 0 and 1 respectively, α is the thermal diffusivity which is equivalent to $k/\rho C_p$, and λ_n are the eigenvalues of the transcendental equation

$$\lambda_n J_1(\lambda_n R) - \frac{h}{k}J_0(\lambda_n R) = 0 \tag{6}$$

To compare with the active cell surface temperature data for the step change from 50°C to 20°C shown in Figure 4, Equation 5 was evaluated at the battery surface ($r = R$) at regular time intervals up to t = 2400 s (40 min) for T_o = 50°C and T_∞ = 20°C. The battery density was measured to be 2721 kg/m^3, which is also consistent with volume and mass values listed in the manufacturer's specifications. For the convective heat transfer coefficient, the type of convection taking place inside the chamber first needed to be determined. The chamber did not contain a fan or mixing device to produce entirely forced convection; however, the battery was situated horizontally underneath a vent that provided some air flow. Therefore, it is reasonable to assume that the heat transfer did not merely occur via free convection either. Since free

convection values for h are around 5-15 W/m^2-K and forced convection values are around 50-100 W/m^2-K [38,40], a median value of 35 W/m^2-K was chosen for this analysis.

Comparison between experimental data and the analytical solution was conducted by varying both k and C_p until the shape and magnitude of values matched as closely as possible. The result of this data fitting is shown in Figure 6, and values found for k and C_p were 0.8 W/m-K and 925 J/kg-K, respectively. There was a clear discrepancy of about 2-3°C between the experimental and analytical data over the first 3 minutes that was likely the result of uneven heat flux while the chamber temperature dropped from 50°C to 20°C. For simplification, it was assumed that at t = 0 the chamber temperature was T_∞ (20°C); however, in reality it likely took the chamber around 30-60 seconds to reach T_∞. Since the boundary condition at $r = R$ (Equation 3) assumed a convective driving force proportional to the temperature difference $T - T_\infty$, the analytical solution showed a steeper initial slope than the experimental data where the actual values for $T - T_\infty$ were smaller for a short time. Additionally, another contributing source of error with this method was the assumed value for h which may have been influenced by the layers of insulating tape holding the thermocouple in place on the battery surface.

The value obtained for k via the analytical data fitting (0.8 W/m-K) was higher than most reported values, and this is likely due to contributions from axial heat flow. While the battery was situated

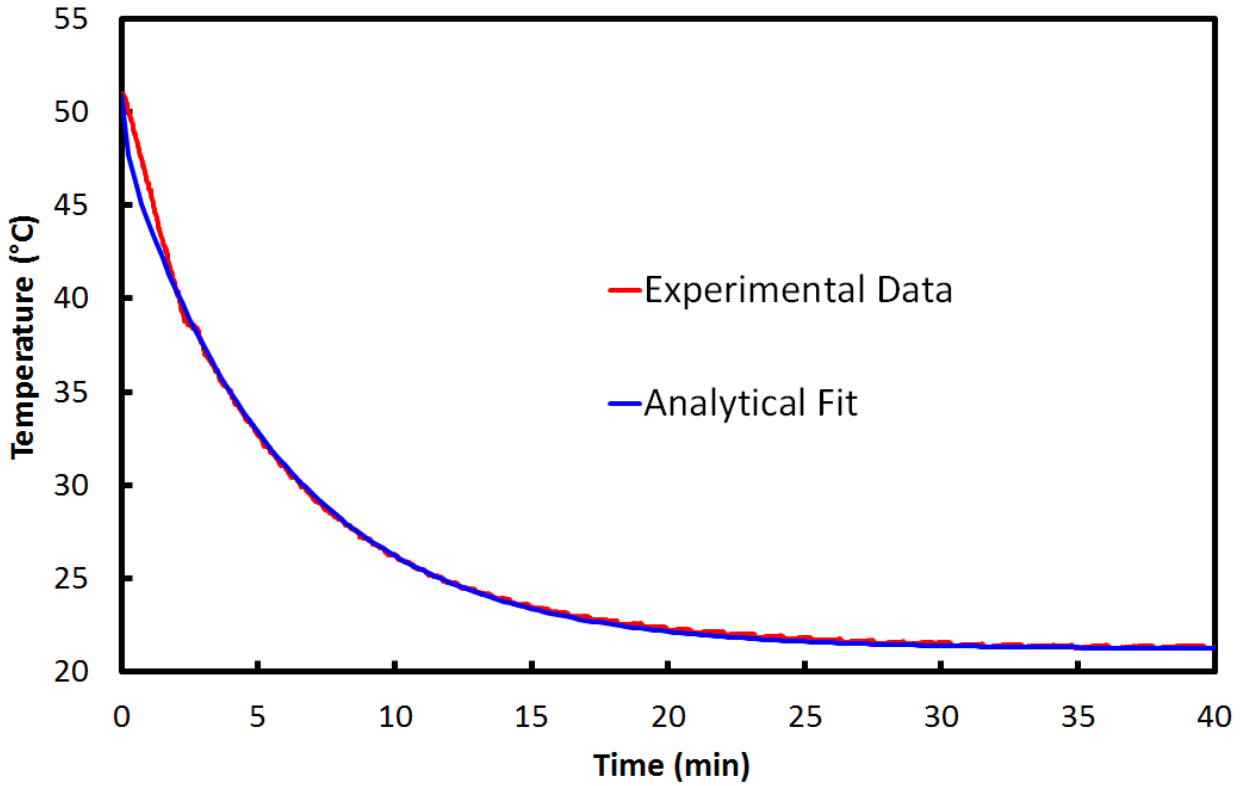

Figure 6. Experimental and analytical fit data for active 18650 battery inside microclimate benchtop temperature test chamber. Data shown for step change from 50°C to 20°C. Temperature of battery measured via thermocouple attached to the surface.

inside the chamber to try and isolate heat flow in the radial direction, ambient air flow likely caused axial propagation as well. Since the axial thermal conductivity is over an order of magnitude higher than the radial thermal conductivity, this axial contribution artificially inflated the value for k. Therefore, to overcome some of these shortcomings associated with the convective analytical method, a second, and more robust, technique that was performed involving external heating combined with numerical analysis. This method offered two distinct advantages compared to the analytical solution just described: (i) it can account for the true, time-dependent heat flux applied to the battery (especially during the initial few minutes); and (ii) heat is applied strictly in the radial direction, allowing a more pure value for radial thermal conductivity to be obtained. In these experiments, an 18650 lithium-ion battery (Tenergy $LiCoO_2$) was wrapped with insulating tape and affixed with a K-type thermocouple (Omega) and micro-foil heat flux sensor (RdF). Nickel-chromium wire (AWG 22) was connected to a power supply and spirally-wound over the length of the battery, and a layer of flexible copper foil was added to distribute the applied heat. After another layer of insulating tape, the whole assembly was loosely wrapped in fiberglass pipe insulation, placed inside a vacuum chamber with feedthroughs for all attached instrumentation, and pumped down to a pressure of 1 psi to minimize convective heat loss. The power supply was turned on to initiate external heating, and the test was stopped once the battery surface temperature reached 50°C. Figure 7 shows the experimentally-measured heat flux during a single trial and illustrates the time-dependent behavior, particularly during the first minute of heating.

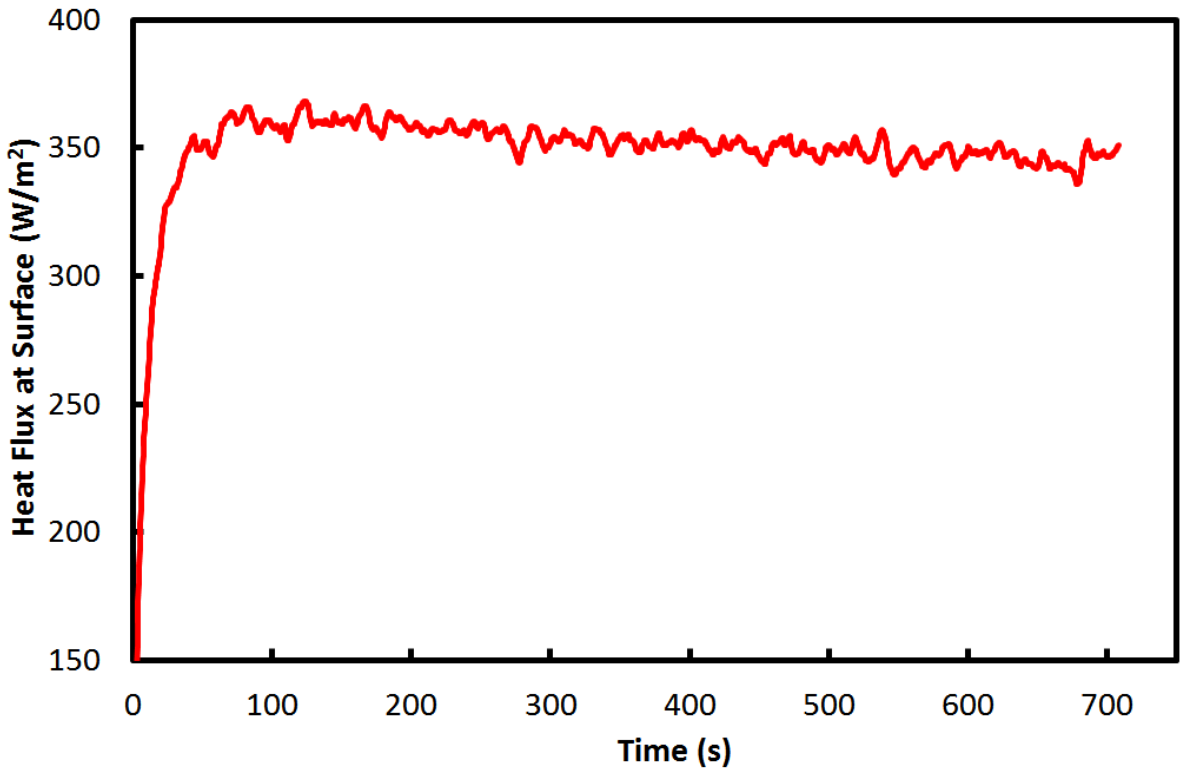

Figure 7. Experimentally measured heat flux into 18650 lithium-ion battery for external heating with numerical analysis test over first 12 minutes.

Numerical analysis was performed by applying a backwards Euler finite difference method to solve the multi-dimensional radial heat equation (Equation 1) with boundary and initial conditions shown in Equations 7-9,

$$\left.\frac{\partial\theta}{\partial r}\right|_{r=0} = 0 \tag{7}$$

$$\left.\frac{\partial\theta}{\partial r}\right|_{r=R} = \frac{Q''}{k} \tag{8}$$

$$\theta(r, t=0) = 0 \tag{9}$$

where in this case the temperature is replaced with θ, the temperature rise ($T - T_o$), and Q" is the applied heat flux. The secant method was then applied to minimize error between experimental data and numerical solutions, thereby extracting accurate estimations of k and C_p. In each trial, a value for C_p was fixed and the secant method was run for approximately 45 iterations until the error was minimized and a value for k converged. A typical example of this procedure is shown graphically in Figure 8 with an arrow indicating the final value for thermal conductivity.

A wide range of values for C_p was selected and this procedure was repeated to generate a plot of multiple solutions for k corresponding to each C_p. This data is shown in Figure 9 for the first trial,

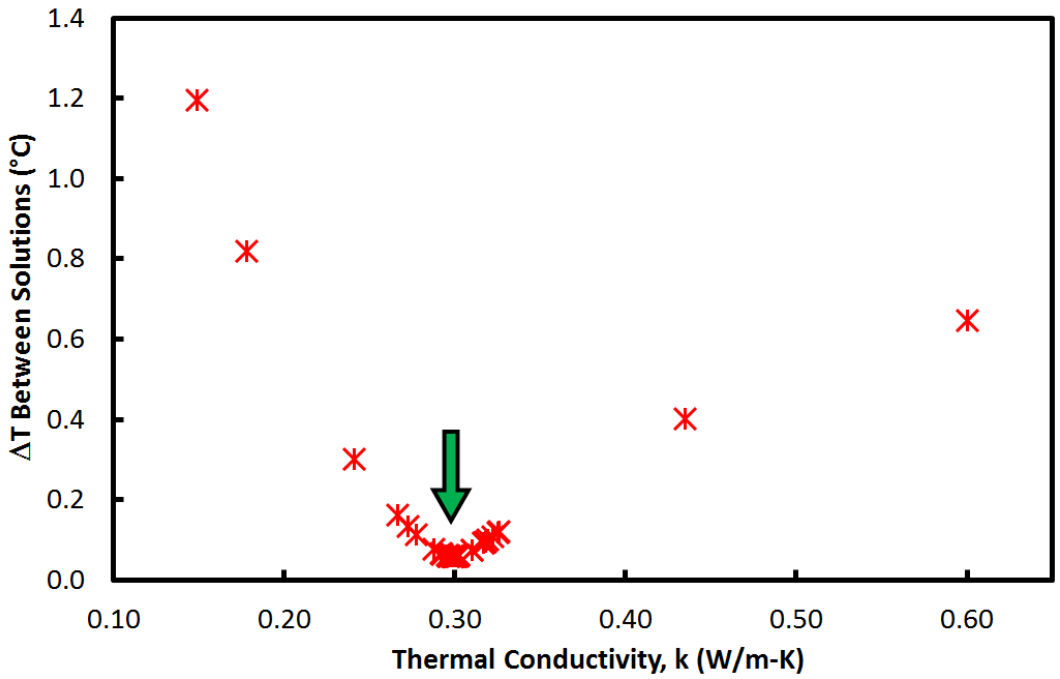

Figure 8. Example of secant method performed for data from trial 1 to obtain thermal conductivity at a fixed heat capacity. Value for thermal conductivity (indicated by green arrow) converged at the lowest error in temperatures between experimental and numerical data.

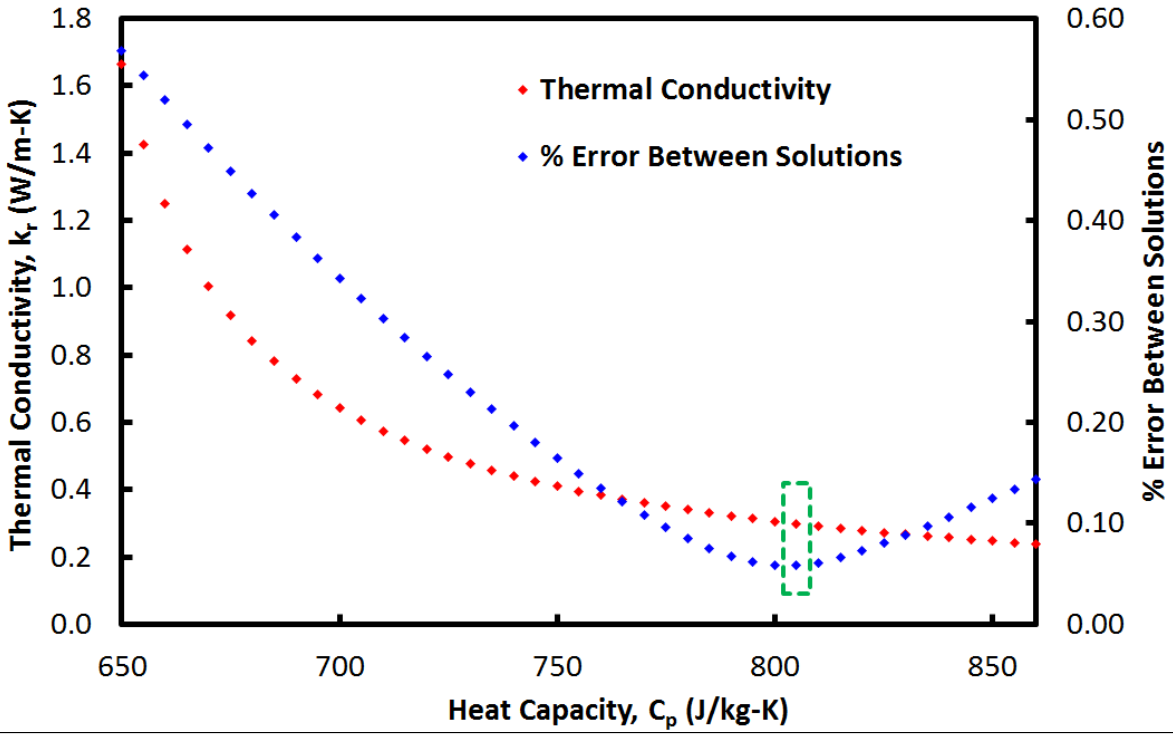

Figure 9. Thermal conductivities obtained via the secant method for a range of fixed heat capacity values from 650 – 860 J/kg-K, along with percent errors between experimental and numerical data for each set of values. Data is from trial 1, and boxed in green is the point where the error was at a minimum, corresponding to the best approximation for thermal conductivity and heat capacity from this trial.

along with the associated errors between experimental and numerical measurements. The best approximations for k and C_p were taken where the error was smallest, and the values from this trial were 0.299 W/m-K and 805 J/kg-K, respectively. Using these values along with the experimental heat flux shown in Figure 7, the temperature rise at $r = R$ for the first 12 minutes was calculated numerically using the previously-mentioned backwards Euler method. This numerical solution was compared with the experimental data, and plots of both are shown in Figure 10. Excellent agreement was observed in Figure 10 between the experimental and numerical curves, particularly for the initial few minutes, highlighting the advantages of this technique and illustrating the capability to accurately capture thermal behavior during periods of transient heat flux.

Nine total trials were conducted and analyzed in a similar manner, and the data is summarized in Table 2. Though different magnitudes of heat flux were applied for each test, there was a high degree of consistency observed in values for k and C_p. Averaging the values over all nine trials gave overall approximations of 0.299 ± 0.013 W/m-K for k and 949 ± 25 J/kg-K for C_p (errors based on standard deviation). The value for C_p was within experimental error of the value obtained via the analytical method (925 J/kg-K), however the value for k obtained from the numerical analysis was much closer to the expected range than the value obtained from the analytical method. Due to the aforementioned advantages of direct radial heating and transient heat flux

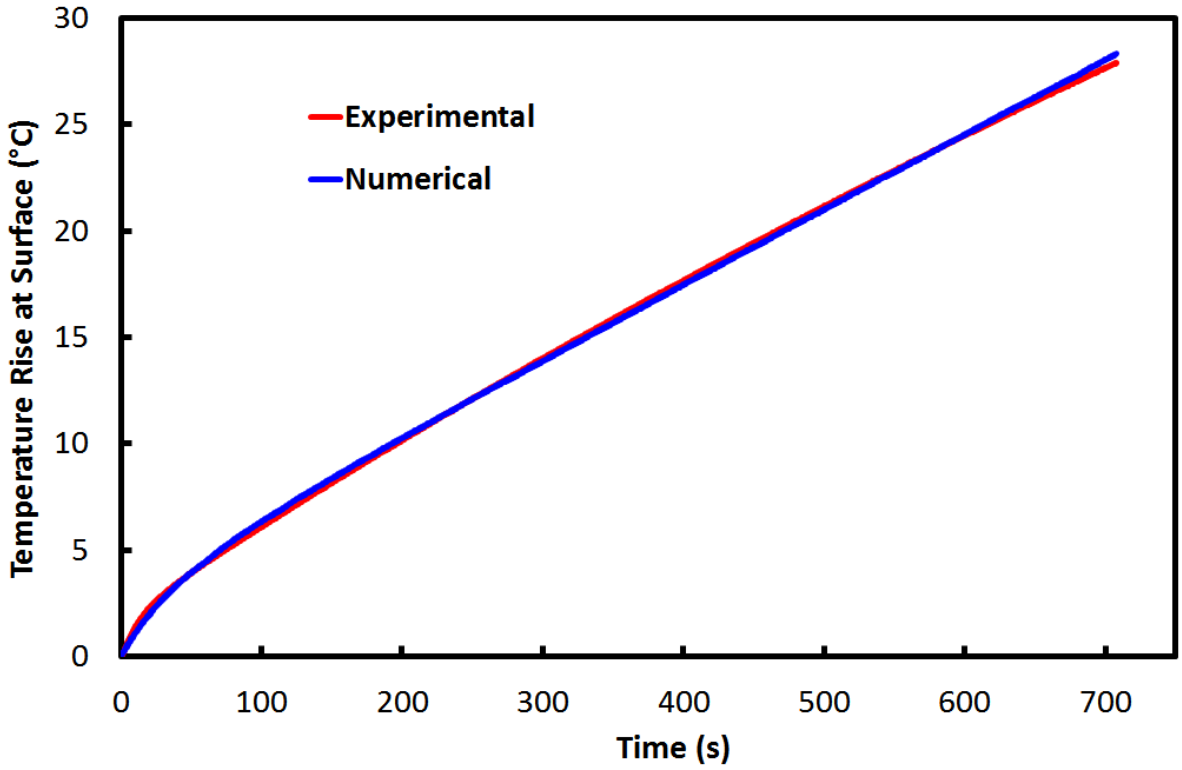

Figure 10. Comparison of temperature rise at the battery surface ($r = R$) vs. time for experimental data and numerical solution using best fit values for thermal conductivity (0.299 W/m-K) and heat capacity (805 J/kg-K) from trial 1. Thermal properties determined by minimizing error via the secant method, and numerical solution obtained through a backwards Euler technique applied to the multi-dimensional radial heat equation.

Table 2. Summary of data from nine external heating and numerical analysis trials on an 18650 $LiCoO_2$ lithium-ion battery. Steady state heat flux measured using a micro-foil heat flux sensor, and thermal conductivity (k) and heat capacity (C_p) values determined via backwards Euler and secant methods applied to the multi-dimensional radial heat equation.

Trial	Steady State Heat Flux (W/m^2)	k (W/m-K)	C_p (J/kg-K)
1	461	0.299	805
2	482	0.301	830
3	486	0.313	825
4	633	0.316	845
5	617	0.317	825
6	593	0.275	795
7	693	0.303	825
8	649	0.274	780
9	658	0.299	800

accountability, the numerical method is preferred over the analytical method for thermal property determination

To verify the accuracy of this external heating numerical analysis method, a material of known thermal properties, polytetrafluoroethylene (PTFE), was used. Table 3 shows the data for steady state heat fluxes and results obtained for k and C_p from all three trials performed. The average values for the thermal properties of PTFE were 0.232 ± 0.003 W/m-K for k and 1203 ± 8 J/kg-K for C_p. Typical literature values for PTFE vary slightly depending on the manufacturer and various physical characteristics, however they are generally reported to be around 0.25-0.30 W/m-K and 1000-1200 J/kg-K for k and C_p, respectively [41-43]. Values obtained for PTFE via this external heating numerical analysis method aligned very closely with reported values, demonstrating the accuracy of this technique.

Table 3. Summary of data from three external heating and numerical analysis trials on a cylinder of polytetrafluoroethylene (PTFE). Steady state heat flux measured using a micro-foil heat flux sensor, and thermal conductivity (k) and heat capacity (C_p) values determined via backwards Euler and secant methods applied to the multi-dimensional radial heat equation.

Trial	Steady State Heat Flux (W/m^2)	k (W/m-K)	C_p (J/kg-K)
1	482	0.230	1195
2	483	0.230	1200
3	483	0.236	1215

The third and final approach that was used to obtain thermal properties was calorimetry. A thermally-insulated Dewar was filled with ~900g of deionized water, and ice was progressively stirred in until the water temperature was between 2-4°C without any residual floating ice. The final mass of water was then recorded. During testing, the Dewar was placed onto a hot plate and a stir bar was added to provide constant stirring and minimize temperature gradients. A beaker with deionized water was also placed onto a separate hot plate and brought to around 80°C under constant stirring. The object under study was submerged in the hot water bath and allowed to equilibrate for at least 30 minutes, followed by rapid transfer into the cold water bath inside the Dewar. Temperatures of the hot and cold water baths were monitored via thermocouples, and the experiment was completed once the temperature rise inside the Dewar resulting from the hot object addition was finished. Values for heat capacity were calculated via a simple heat balance using the initial water and object temperatures, the final water temperature, and the water and object masses.

Before conducting any tests, the cold water bath temperature rise inside the Dewar resulting from ambient heat transfer was measured. The temperature rise over time in the range from 4-8°C was found to be linear, and the data is shown in Figure 11. From the slope obtained via linear

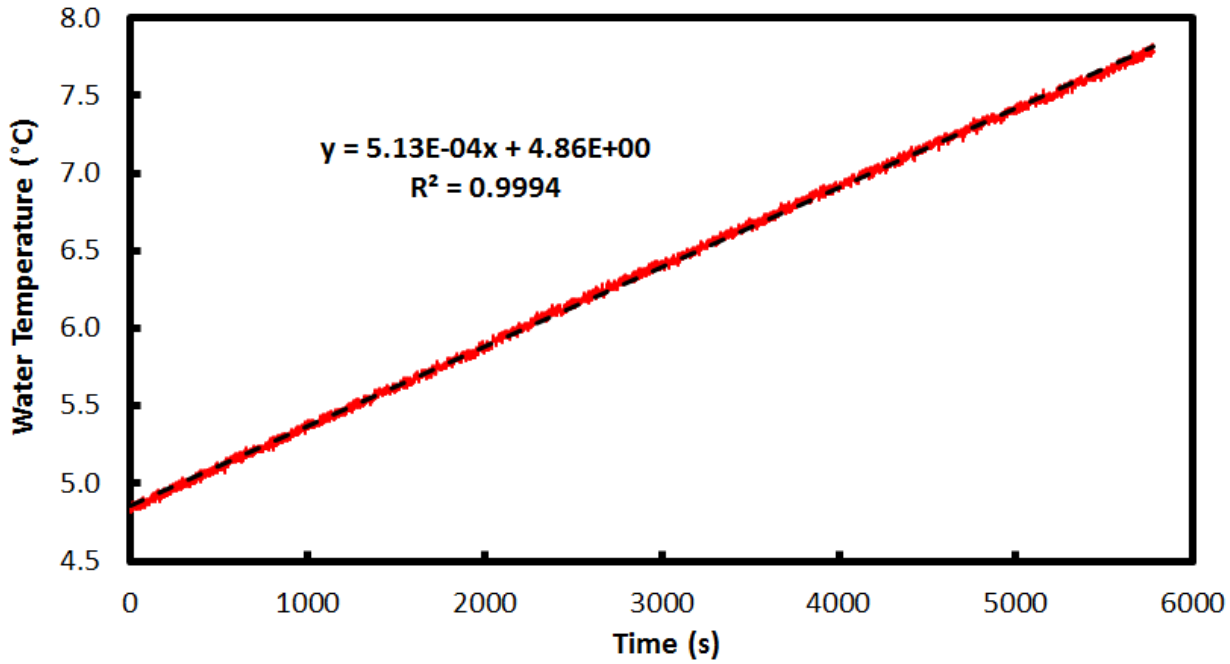

Figure 11. Ambient water temperature rise inside thermally-insulated Dewar between 4-8°C along with linear regression.

regression as shown in Figure 11 (5.13 x 10^{-4} °C/s), the intrinsic temperature rise of the calorimeter was thereby determined. The final temperature for all calorimetry tests was within this 4-8°C range, and the water temperature was considered to be finally equilibrated once the time-averaged temperature rise dropped to this value. An example of the water bath temperature and 30 second-averaged temperature vs. time slopes for a $LiCoO_2$ trial is shown in Figure 12 with a vertical green line indicating the point at which the slope dropped consistently to the experimentally-measured ambient temperature rise value and the final temperature was taken.

Calorimetry tests were conducted using PTFE, aluminum type 6061, and commercial 18650 $LiCoO_2$ lithium-ion batteries. It was not practical, however, to perform such tests with active 18650 cells due to the risk of water infiltration and/or short circuiting while the batteries were submerged in water for extended periods of time. Therefore, in order to render the batteries safe for these tests, they were initially placed inside the microclimate benchtop temperature test chamber, heated to ~100°C, and allowed to rest until there was a severe drop in the open circuit voltage triggered by activation of the shutdown separator safety device. The shutdown separator is designed to melt and distribute throughout the separator in the jelly roll, clogging the pores that allow Li^+ transport between anode and cathode and effectively causing permanent deactivation of the battery [44]. The benefit of this strategy is that no disassembly, overcharge, or severe overheating was necessary, and therefore it was assumed that the thermophysical properties of the battery remained largely unaffected.

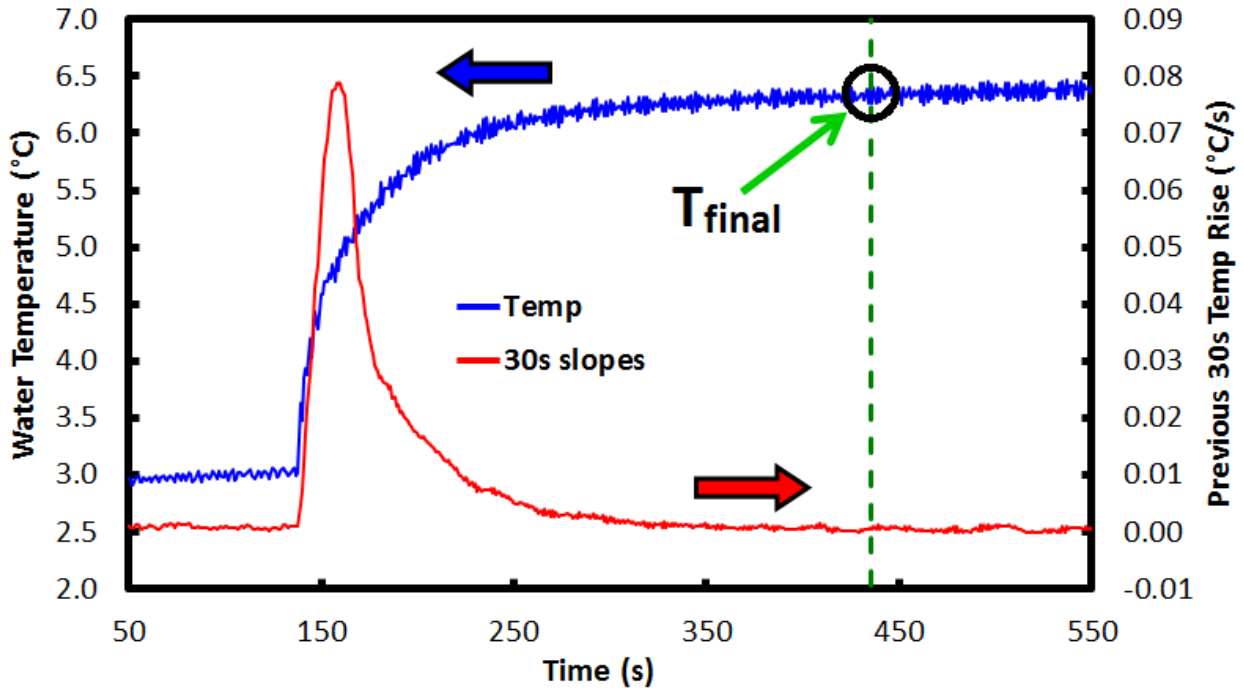

Figure 12. Temperature vs. time (blue line, left axis) and running 30-second average temperature-time slope (red line, right axis) calorimetry data for single trial of $LiCoO_2$. Vertical green line denotes point at which 30-second temperature rise dropped consistently to the ambient value (5.13×10^{-4} °C/s) of the calorimeter, and corresponding final temperature indicated.

Table 4 shows the average values for C_p obtained from calorimetry experiments for all three materials, along with typical values for each reported in the literature. All values of C_p fell within the expected range of reported values. However, all three C_ps obtained were in the lower range of values for each material, suggesting that this calorimetry method may have had a minor but consistent source of error that caused slight underestimation in the calculated values for C_p. This point was also evident when comparing calorimetry values with those obtained from the numerical and analytical methods. For PTFE, the calorimetry value (1073 ± 17 J/kg-K) was about 11% lower than the numerical analysis value (1203 ± 8 J/kg-K), and for the 18650 lithium-ion batteries the analytical value (925 J/kg-K) was only about 3% higher than the calorimetry value (896 ± 31 J/kg-K). However, this trend was not observed with respect to the numerical technique value for the 18650 $LiCoO_2$ battery (814 ± 19 J/kg-K), which was slightly lower than the calorimetry value. Generally, despite minor differences, C_p values obtained across all methods were very similar, and correlated closely to reported literature values. A summary of values is also shown in Table 5. The work in this section is also being drafted into a manuscript for publication in a peer-reviewed scientific journal [45]. Determination of these properties will be crucial for the development of accurate thermal and electrochemical models aimed at predicting battery behavior leading up to thermal runaway and potential energetic failure events.

Table 4. Values for heat capacity (C_p) obtained via calorimetry compared to reported values in the literature of aluminum (type 6061), PTFE, and typical 18650 commercial lithium-ion batteries. Sources: a – [18]; b – [27]; c – [29]; d – [30]; e – [35]; f – [36]; g – [37]; h – [41]; i – [42].

	C_p (J/kg-K) of Material		
	Aluminum	**PTFE**	**18650 Li-ion Battery**
Calorimetry	860 ± 8	1073 ± 17	896 ± 31
Literature	860-890[c,d]	1000-1200[h,i]	800-1700[a,b,e,f,g]

Table 5. Summary of values for heat capacity (C_p) and thermal conductivity (k) of commercial $LiCoO_2$ 18650 lithium-ion batteries obtained via three methods (analytical analysis, numerical analysis, and calorimetry), in addition to typical values reported in the literature. Sources: a – [18]; b – [27]; c – [35], d – [36]; e – [37]; f – [38].

	Analytical	**Numerical**	**Calorimetry**	**Literature Reported Values**
C_p (J/kg-K)	925	814 ± 19	896 ± 31	800-1700[a,b,c,d,e]
k (W/m-K)	0.8	0.300 ± 0.015 (radial)	--	0.2-2.0 (radial)[a,b,c,d,f] 30 (axial)[a,b,c,f]

3.3 EIS-based Non-Invasive Internal Temperature Determination

Temperature monitoring of active lithium-ion batteries, particularly in a large format battery pack, is crucial. Overheating to extremely high temperatures (130-200°C) can result in unwanted exothermic reactions, battery shutdown, and potentially catastrophic thermal runaway [18,46-48]. Extremely low temperatures (as low as 0°C to -40°C) can be equally problematic as well, especially during charging, with lithium metal plating and high interfacial resistances contributing to poor performance and possible failure [9,18,28,49-51]. Typical methods used for battery temperature monitoring involve thermocouples attached to the outside of the battery, which provides only surface temperature measurements. This is a significant issue since the internal temperature of a battery is far more critical and relevant with respect to detecting the onset of a failure event than the surface temperature, particularly because as a battery experiences rapid overheating the surface temperature is often much lower than the internal temperature [27,28,52-54]. Therefore, merely surface temperature monitoring by itself is likely not effective enough to adequately probe the internal thermal conditions of a battery, nor accurately predict the onset of a failure event.

Several recent works have investigated the use of Electrochemical Impedance Spectroscopy (EIS) for non-invasive determination of the state-of-health and/or internal temperature of lithium-ion batteries [16,48-50,53,55-57]. This technique is particularly attractive for several

reasons: (i) EIS measurements do not require battery disassembly or physical insertion of a thermocouple but rather can be performed on fully-intact cells; (ii) it is virtually instantaneous (<1 second); and (iii) it can be applied to any lithium-ion battery chemistry or cell geometry. Various correlations have been demonstrated that take advantage of different EIS-measured properties, including the phase angle (ϕ), imaginary impedance ($-Z_{imag}$), and charge-transfer resistance (R), illustrating the dynamic potential for this technique to provide meaningful results in a number of ways. Common to these reports is the critical observation that impedance is independent of the battery's state of charge (SOC) and only a function of temperature for a certain frequency range [16,36,48-51,53]. In this frequency range (typically ~100-1000 Hz depending on the battery), the impedance corresponds primarily to the solid-electrolyte interphase (SEI) on the anode surface, which carries no charge and is therefore unaffected by the SOC [48,49,58]. Hence, in this study EIS was performed to obtain correlations with the internal temperature of an active lithium-ion battery, and this work will be used to enable real-time internal temperature monitoring in future battery failure tests.

Commercial $LiCoO_2$ 18650 lithium-ion batteries (Tenergy) were used along with the microclimate benchtop temperature test chamber. EIS spectra were collected in 5°C increments from -10°C to 95°C for the entire range of SOCs, and multiple batteries were used to collect this data to ensure homogeneity and consistency among different cells. The battery was first fully charged at C/13 (100% SOC) at 20°C, followed by a 4 hour rest at open circuit while the chamber heated or cooled to the desired temperature. After this time, it was safely assumed that the battery had equilibrated completely with the chamber, and the internal temperature could be assumed to be constant. Chamber and battery surface temperatures were also monitored via thermocouples since it was observed (in previous, separate tests) that slight disparities existed between the chamber set point and the actual chamber temperature. EIS was then measured at the same temperature between 30000 – 0.01 Hz with a 40 mV perturbation for every 10% SOC. After each EIS test, the battery was discharged 10% (duration of 1.3 hours) at C/13 followed by a 30 minute rest period. Once 0% SOC was reached and the final EIS spectrum was collected, the chamber was reset to 20°C and the battery was again charged to 100% SOC before tests at the next temperature were started. Charging was carried out at ambient conditions to ensure safety because extreme temperatures – both high and low – pose significantly greater challenges during charging than discharging.

Nyquist plots were produced for each temperature by taking averages of the real and imaginary impedances (Z_R and $-Z_{imag}$) for all SOCs from 0-100%, and this data along with standard deviation error bars are shown in Figure 13. Typical lithium-ion battery behavior was observed in Figure 13: inductance in the high frequency region up until the Z_R axis intercept (leftmost side of the plots), a semicircle corresponding to the SEI and Li^+ transport in the middle frequency region, and an inclined line resulting from the Warburg impedance and diffusional effects in the low frequency region [59,60]. A trend in error bar magnitudes was seen for all temperatures that was consistent with the expected behavior that impedance is unaffected by SOC. Standard deviations for both Z_R and $-Z_{imag}$ were largest at both ends of the frequency spectrum and reached minima in the 100-

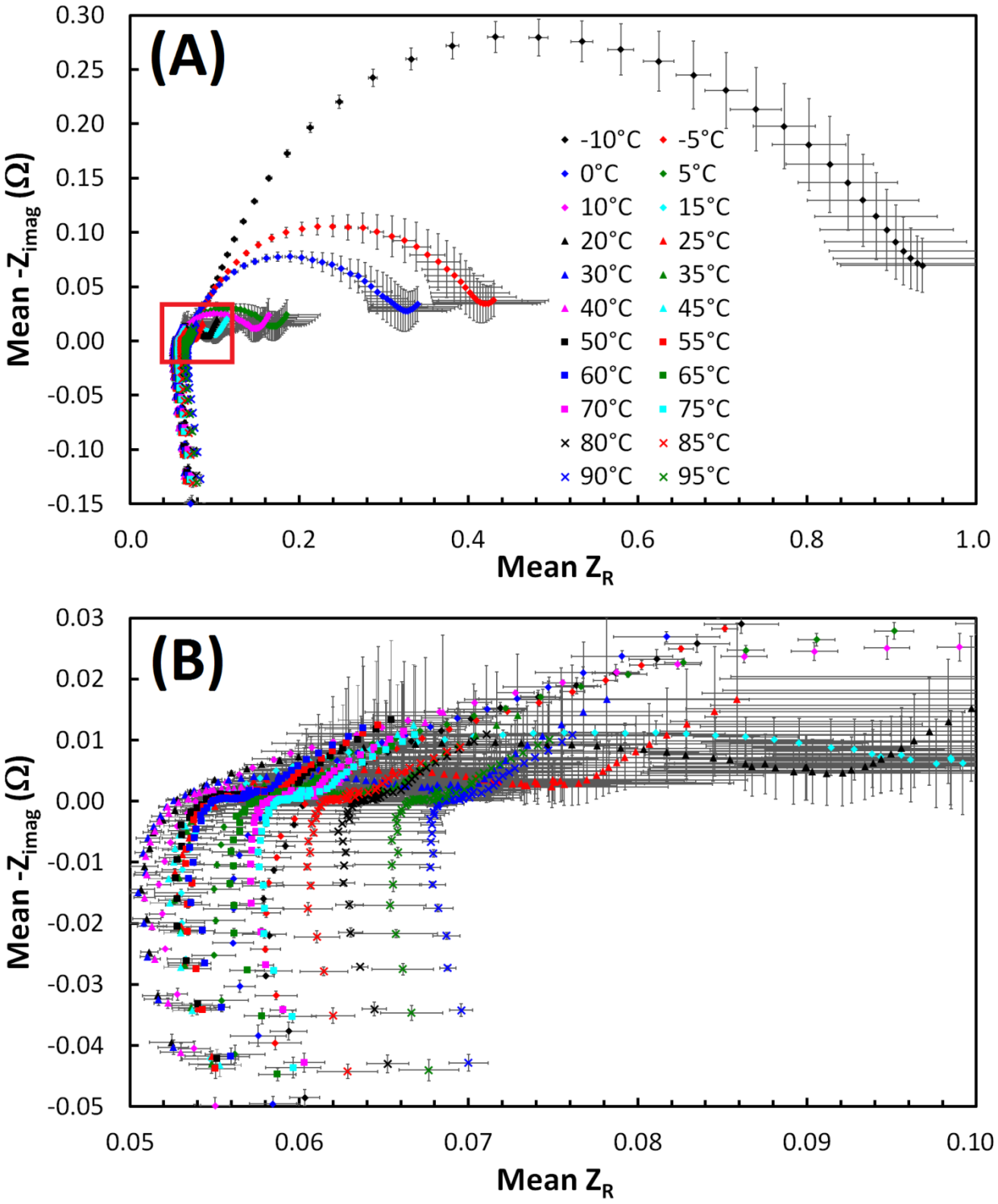

Figure 13. EIS Nyquist plots for Tenergy 18650 $LiCoO_2$ lithium-ion batteries averaged for every 10% state of charge from 0-100%. Data obtained for temperatures between -10°C and 95°C at 5°C increments, and error bars represent standard deviations in $-Z_{imag}$ and Z_R across all states of charge for each temperature. (A) shows entire range, and (B) shows zoomed in section denoted with a red box in (A).

1000 Hz range, corresponding to the SEI charge-transfer resistance. In particular, $-Z_{imag}$ displayed a strong temperature dependence, and Figure 14 shows the full and selected frequency ranges of $-Z_{imag}$ values for each temperature vs. frequency. The two frequencies that exhibited the smallest overall standard deviations across all SOCs, 300 Hz and 949 Hz, were identified, and Figure 15 shows the temperature-dependent plots along with the best fit correlations for each. For temperatures between -10°C and 55°C, an Arrhenius-like dependence, Equation 10, was observed for the plot of $-Z_{imag}$ vs. internal temperature (Figure 15A), and the parameters *A*, *B*, and *C* were determined via least-squares analysis.

$$-Z_{imag} = Ae^{\frac{B}{T}} + C \tag{10}$$

For the higher temperature correlation (60°C to 95°C), the overall impedance magnitude (Z_{mag}) was used because it displayed a stronger temperature dependence than $-Z_{imag}$ in this temperature range, and this trend is seen clearly in Figure 15. An empirical, simple exponential best fit curve was applied for this correlation, Equation 11,

$$-Z_{imag} = Ae^{BT} + C \tag{11}$$

and the values for *A*, *B*, and *C* for both low and high temperature correlations, along with corresponding units, are listed in Table 6. For the low temperature best fit curve, comparing the exponential term in Equation 10 with the parameters in an Arrhenius-type expression, Equation 12,

$$-Z_{imag} = Ae^{\frac{E_a}{RT}} \tag{12}$$

where E_a is the activation energy and *R* is the ideal gas constant, an estimate for E_a was found to be 0.13 eV. This value was slightly lower than commonly reported values (typically ~0.2-0.4 eV), and this activation energy has been attributed to the ionic conductivity of the SEI [48,49]. Therefore, it is apparent that the Tenergy $LiCoO_2$ 18650 batteries used in this study exhibited above-average SEI characteristics compared to other commercial cells.

To further illustrate the accuracy of the Arrhenius-type fit for the low temperature correlation, Equation 10 was rearranged into a linear form, Equation 13:

$$\ln\left(-Z_{imag} - C\right) = \ln A + \frac{B}{T} \tag{13}$$

A plot was then made of $\ln(-Z_{imag} - C)$ vs. $1/T$, and the result is shown in Figure 16. The linear regression shown in Figure 16 fit the data very closely, and the values obtained for *A* and *B* were almost identical to the values determined via least squares analysis for the Arrhenius expression shown in Table 6.

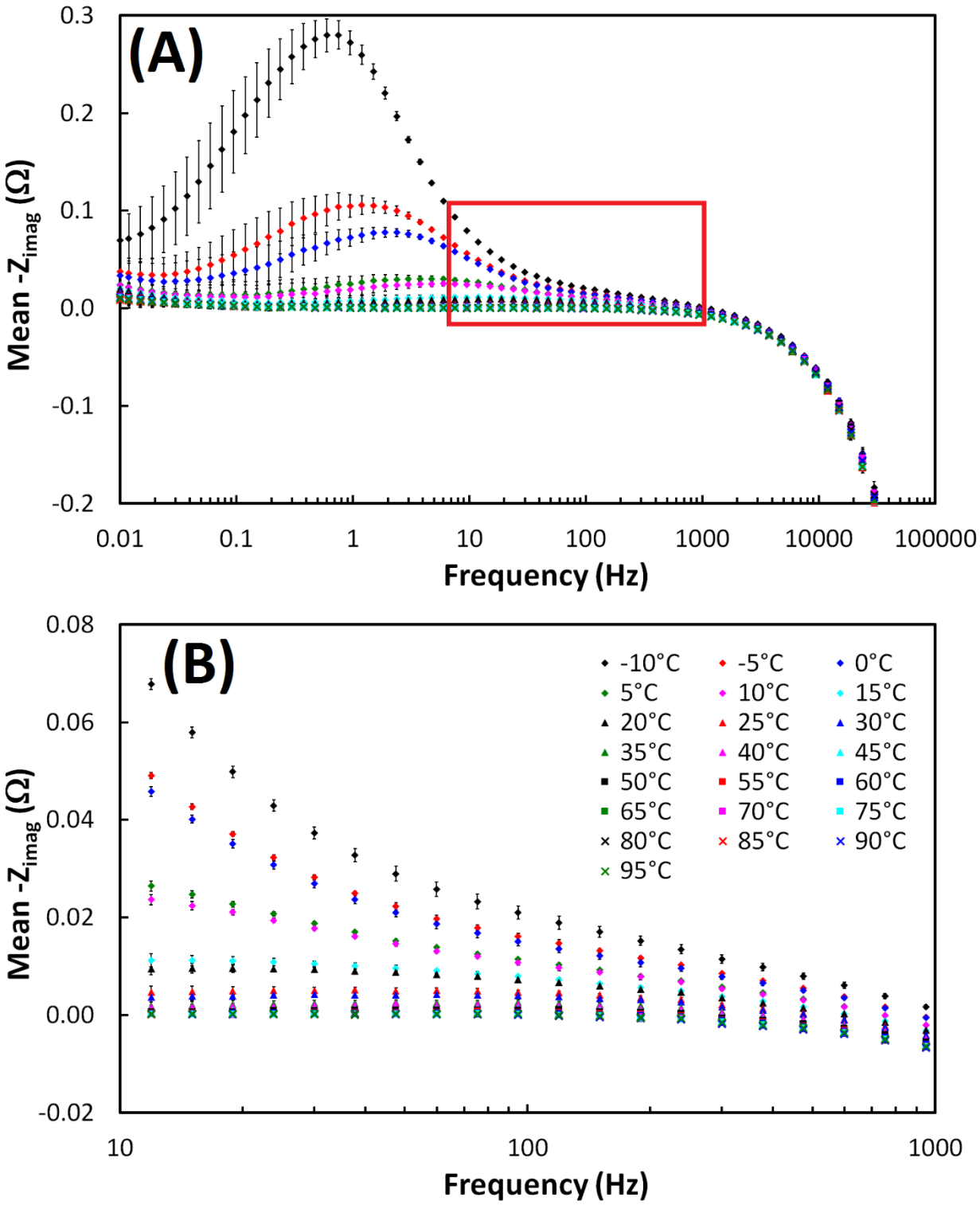

Figure 14. State of charge-averaged imaginary impedance ($-Z_{imag}$) vs. frequency for Tenergy 18650 $LiCoO_2$ lithium-ion batteries for temperatures between -10°C and 95°C at 5°C increments, and error bars represent standard deviations across all states of charge for each temperature. (A) shows entire range, and (B) shows zoomed in section denoted with a red box in (A) for specific range between 10-1000 Hz.

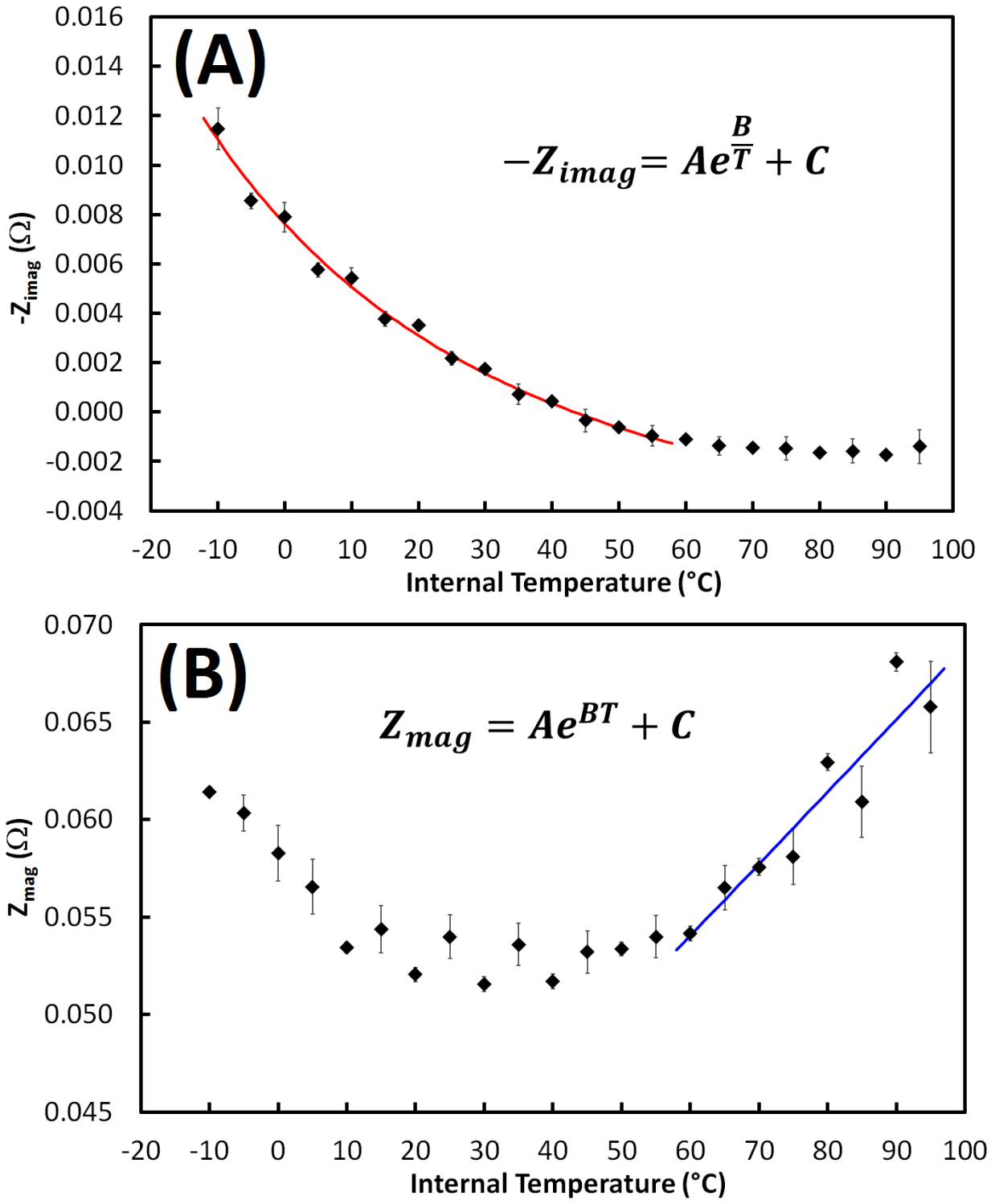

Figure 15. Internal temperature-dependent correlations for Tenergy 18650 $LiCoO_2$ lithium-ion batteries. (A) shows the imaginary impedance vs. temperature correlation for the range -10°C to 55°C, along with an Arrhenius-like dependence and best fit curve. (B) shows the overall impedance magnitude vs. temperature correlation for the range 60°C to 95°C, along with an exponential dependence and best fit curve. Best fits were determined using a least squares analysis.

Table 6. Best fit curve parameters determined via least squares analysis for low and high temperature impedance correlations for Tenergy 18650 $LiCoO_2$ lithium-ion batteries.

	A	B	C
Low Temperature Range (-10°C to 55°C) (Arrhenius)	$5.041 \times 10^{-5}\ \Omega$	1540 K	-0.006553 Ω
High Temperature Range (60°C to 95°C) (Exponential)	0.4822 Ω	$0.0006180\ K^{-1}$	-0.5383 Ω

Validation of the impedance-temperature correlations was performed via single-frequency tests at various temperatures. A fresh 18650 $LiCoO_2$ battery was placed inside the microclimate benchtop temperature test chamber and a series of temperature set points were programmed in an arbitrary order with 2 hour rest periods to allow equilibration. Surface-attached thermocouples were used to measure the actual battery temperature, and Figure 17 shows the temperatures

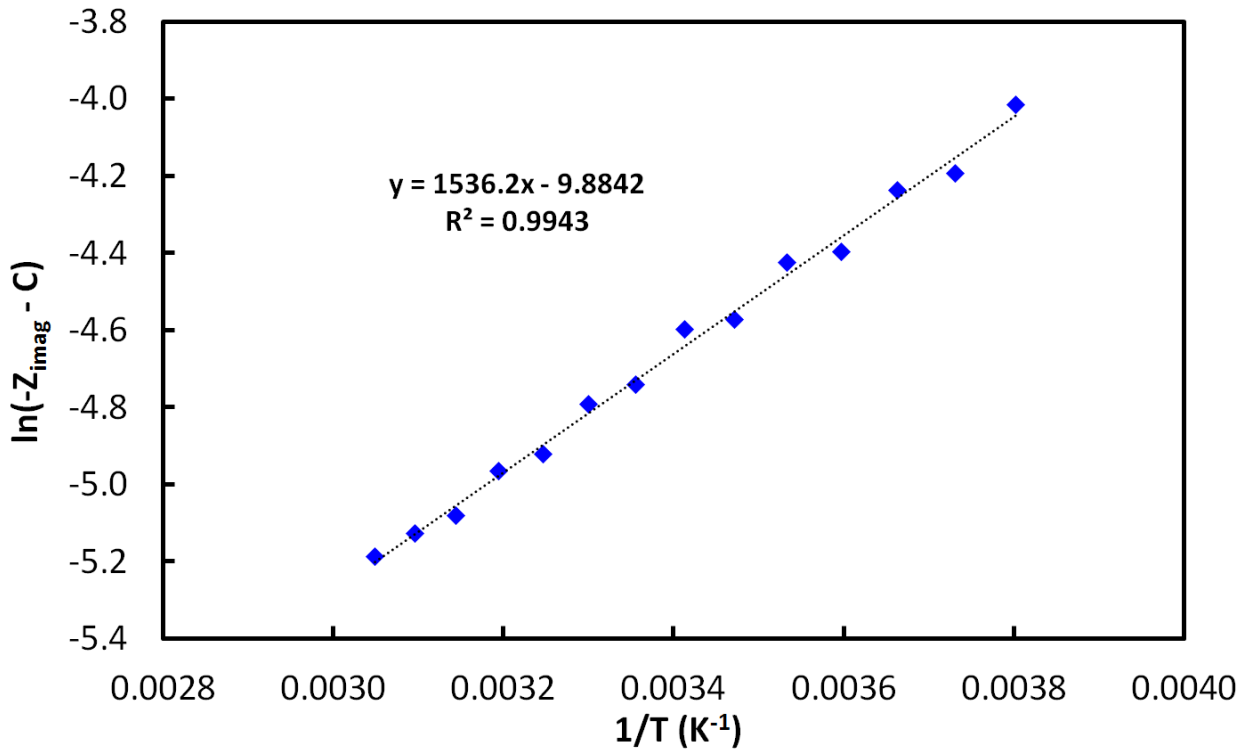

Figure 16. Linear rearrangement of Arrhenius-like equation (Equation 10) for low temperature impedance correlation of Tenergy 18650 $LiCoO_2$ batteries, along with linear regression trendline.

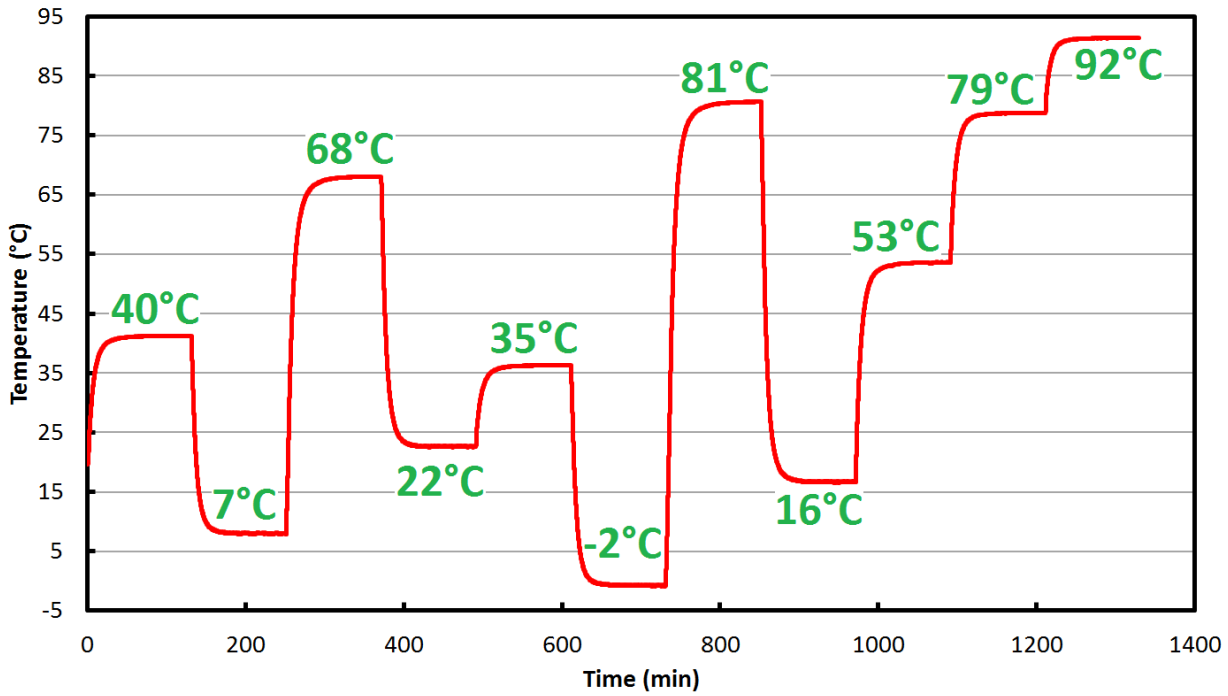

Figure 17. Battery surface temperatures monitored for single-frequency EIS tests of Tenergy 18650 $LiCoO_2$ batteries. Battery was allow 2 hours rest at each temperature to ensure equilibration of internal temperature with chamber temperature, and EIS experiments were conducted at the end of each 2 hour rest period.

monitored over time for this test. Single-frequency EIS data was collected at the end of the each 2 hour rest period at either 300 Hz or 949 Hz, depending on the temperature range. Two separate experiments were conducted with this temperature program: the first consisted of a single EIS test for each temperature, and the second consisted of five EIS tests for each temperature. This allowed for comparison of a single value for impedance parameters with an average or minimum/maximum of the five values. The benefit of this technique, as previously-mentioned, is that five EIS tests carried out at 300 Hz is still virtually instantaneous compared to one EIS test, therefore there is no detriment to taking more data points as needed.

$-Z_{imag}$ and Z_{mag} values from the low and high temperature ranges, respectively, were used with the parameters in Table 6 and Equations 10 and 11 to obtain experimental estimates of the battery internal temperature. Estimates were obtained three ways: first, using the single EIS test impedance results; second, using an average of all impedance values from the five EIS tests; and third, using the minimum $-Z_{imag}$ and maximum Z_{mag} values from the five EIS tests for the low and high temperature correlations, respectively. The minimum/maximum strategy was used in an effort to improve accuracy based on an initial observation that fit temperatures were consistently falling below actual temperatures. Table 7 lists the actual battery temperatures alongside the fit temperatures for all three methods, and Figure 18 shows plots of fit vs. actual temperatures for the low and high ranges, as well as charts displaying the temperature differences between actual and fit values.

Table 7. Actual and EIS fit temperatures obtained via three methods: one point impedance values, average of five impedance values, and minimum imaginary impedance (low temperature range)/maximum overall impedance magnitude (high temperature range) of five impedance values. Bold demarcation in table indicates separation between low and high temperature ranges.

One Point		Five Points - Average		Five Points - Min/Max	
Actual (°C)	Fit (°C)	Actual (°C)	Fit (°C)	Actual (°C)	Fit (°C)
-0.8	-2.7	-0.7	-1.7	-0.7	-1.1
7.9	5.1	8.0	6.9	8.0	7.9
16.7	15.0	16.9	14.6	16.9	15.5
22.7	19.7	22.7	19.9	22.7	20.6
36.3	32.4	36.4	32.9	36.4	33.8
41.2	35.0	41.2	39.6	41.2	40.4
53.6	50.0	53.6	48.9	53.6	49.8
68.1	59.8	68.2	61.4	68.2	61.9
78.8	63.5	78.7	66.2	78.7	67.0
80.7	65.2	80.7	66.9	80.7	67.7
91.5	74.9	91.3	75.9	91.3	77.0

As shown in Figure 18, great overall accuracy was observed for the low temperature range, especially for the minimum/maximum method which exhibited (with just one exception) the closest fits and consistently showed only ~2°C or lower difference between actual and fit temperatures. The high temperature range, however, presented the biggest challenges to accurate impedance-based internal temperature monitoring. The closest fit was still over 6°C below the actual battery temperature, and differences reached as large as 16°C for the highest temperature (92°C). Even despite the large discrepancies, however, the minimum/maximum method was once again the most accurate amongst the three. Additionally, one positive sign from the high temperature data was that the trend of increasing fit temperature as the actual temperature rose was maintained, suggesting that a secondary, or else entirely separate, correlation may be possible that enables more accurate data fitting. This will be investigated more thoroughly in the future, and the current work is being drafted into a manuscript that will be submitted for publication in a high impact scientific journal [61].

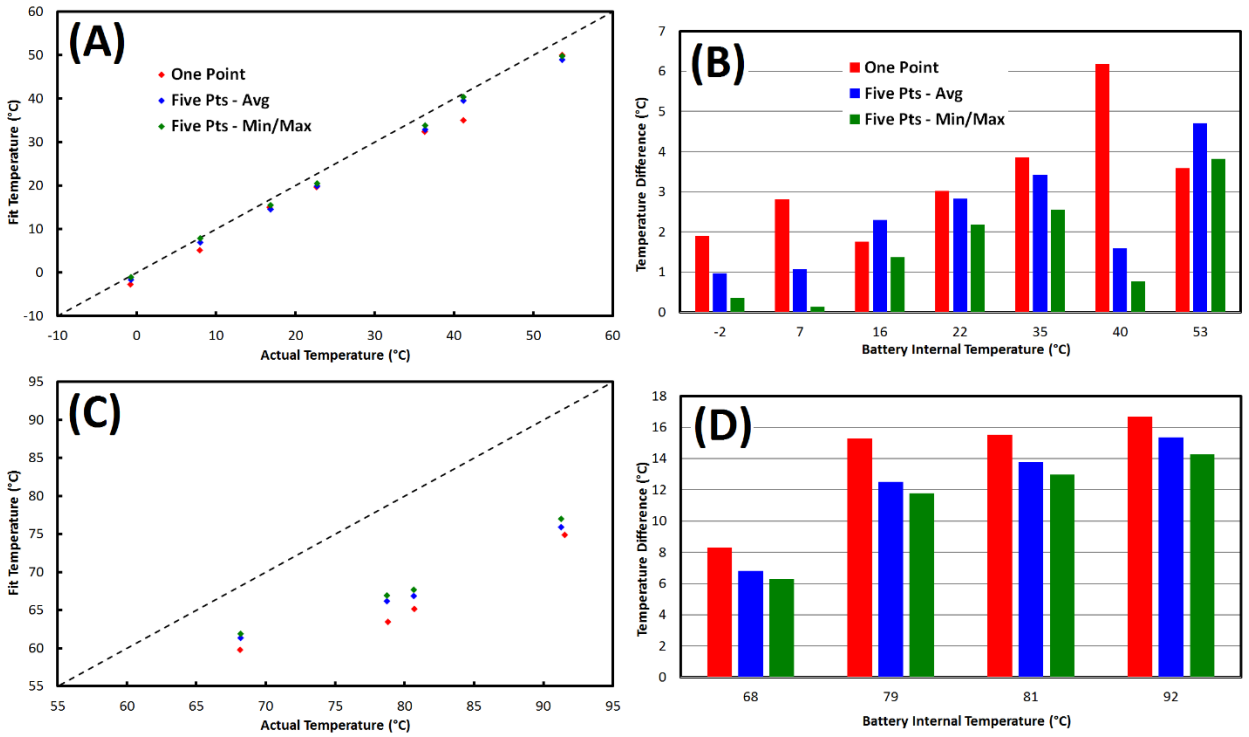

Figure 18. (A) shows plot of fit temperature vs. actual temperature and (B) shows differences between fit and actual temperatures for the low temperature range. (C) and (D) show similar data for the high temperature range. Fit temperatures obtained via three methods: one point impedance values, average of five impedance values, and minimum imaginary impedance (low temperature range)/maximum overall impedance magnitude (high temperature range) of five impedance values.

The data shown in this section opens new doors for real-time monitoring of active battery internal temperature leading up to a failure event. Combining EIS-based temperature measurements with cell-to-cell failure tests will enable a greater level of understanding of battery behavior, and it will also aid in the collection of data to be fed into predictive models. Further analysis of impedance spectra will be crucial as well to elucidate contributions from both overheated and overcharged cells, and the goal is implementation of a single-frequency, instantaneous EIS test to obtain all aspects of a battery's state of health at any moment. This kind of tool could prove to be critical for the safety of single and large format batteries, and future work will be aimed at accomplishing this goal.

3.4 Multi-Cell Model Development and Analysis

Most existing computational models of heat transfer consider Joule heating and electrochemistry that occurs during normal operation of a battery [62-64]. They consider the effects of overcharging on the heat release that results in an extremely slow (0.001°C/min) temperature rise, and a total temperature rise of less than 40°C. Some of the models were compared with experimental measurements for different cell chemistries and materials. Many of these models

considered internal details of a single cell rather than a cell pack, and are focused on the material design of cell contents for safe operation.

Very few well-validated models are available in the literature that consider self-heating and thermal runaway at temperatures above 60°C, and are also focused on mitigation, damage control, and fire safety. The National Renewable Energy Laboratory (NREL) developed a network model that simulates anisotropic conductive heat transfer among cells and air gaps between the cells in a cell pack [65]. Heat loss from cell surfaces was modeled using heat transfer coefficients, which were based on classical, steady-state, empirical correlations for Nusselt numbers developed for general heat transfer in laminar or turbulent flows rather than for transient heating of battery cells.

Specifically, there are a lack of models that consider the phenomena that were evident in experiments described in our previously-published work [26]. The existing models do not consider experimentally-measured decomposition and combustion kinetics that occur inside a cell at high temperatures. Instead, they fit Arrhenius parameters for an assumed global reaction to the experimental measurements of temperature rise in an active cell [65]. There is also a lack of experimental data on the decomposition of electrolyte, electrodes, and the release of gases, particularly oxygen. The oxygen released inside the cell can react with metal electrodes causing enormous heat release due to the internal combustion. There is also a lack of understanding of the pressure rise leading to cell rupture. NREL's model also ignores the dynamics of buoyancy-driven fluid flow in the surrounding air. This is critical with respect to how heat spreads vertically from a battery pack. Perhaps even more important, the models do not consider venting of liquid, gas, and other solid particles from a ruptured cell that affects heat spread, which was evident in our previous work. This is crucial because the vented material can be flammable and hence ignited by the buoyancy flow of hot air, thereby causing fire spread. Furthermore, neither experimental data nor models are available that describe the chemical and thermal properties of materials during the decomposition and combustion of cell contents. Finally, there are a lack of models that are verified in detail against experimental measurements for self-heating and thermal runaway.

This year, we have developed a computational model that considers: (i) experimentally-measured heat release rates from an active 18650 $LiCoO_2$ lithium-ion battery at temperatures up to 300°C under adiabatic conditions; (ii) heat transfer to thermally well-characterized surrogate cells; (iii) heat transfer through buoyancy-driven flow in surrounding air; and (iv) comparison of model predictions for self-heating of the active cell up to the point of thermal runaway (around 250°C) with experimental data. We have not yet modeled the pressure rise inside a cell and its rupture. We also have not, at this point, modeled venting of material from a ruptured cell, nor the ignition of the vented material and the ensuing fire.

In our model development, we made the following assumptions:

(1) The calorimetric measurements of adiabatic self-heating rates for an uncharged, full cell describe the heat generation rate due to decomposition and internal combustion in a closed cell; the effects of SOC on the self-heating rate is negligible at elevated temperatures (>100°C).

(2) The electrochemical (Joule and Faraday) heating are important at low temperatures but have negligible effects compared to that of thermal decomposition of active cell contents at temperature greater than 100°C; the measured rates of temperature rise increase by orders of magnitude at higher temperatures.

(3) The cell remains a closed system until the point of rupture. All cell contents are vented instantaneously from the cell at the peak temperature measured in the experiments. When venting occurs, the heat release from the cell ceases without ignition or fire spread.

With these assumptions, we developed a computational model for thermal runaway of an active cell placed at the center of a pack of eight inactive, surrogate cells. In the numerical model, the cells overlapped by about 1 mm to achieve good contact. In the experiments, cells were pressed together and held in place by glue to achieve the desired contact. The surrogate cells were assumed to be made of aluminum, and minor contributions in thermal properties from the stainless steel casing and cap were therefore neglected. As described in the experiments [26], we considered external heating of an active cell for a fixed time period (1320 s) to initiate the self-heating in the computational model. One of the surrogate cells contained the external heater similar to the experimental setup. The model calculated the heat spread initially from the heater cell to the active cell until the initiation of thermal runaway. This was followed by heat spread from the active cell to all adjacent cells including the heater cell during thermal runaway. We compared the model predictions for temperature and heat flux with experimental data. By verifying the model with our experimental data, it can be used to assess future fire threats posed by active cell packs.

Previous experimental work showed the temperature and heat flux at the surface of the active cell during the initiation of self-heating by the heater cell and the thermal runaway that follows. Figure 19 shows that the temperature rose with time as the heater cell was turned on. The rate of temperature rise was high initially and then decreased with time. After some time, the rate of temperature rise increased dramatically for a short period of time before falling off to near zero. The complex behavior exhibited by the temperature rise was the result of three effects: (i) heat generated by the decomposition of all contents in the active cell (separator, electrodes, and electrolyte); (ii) heat input into the heater cell; and (iii) heat loss to the adjacent surrogate cells and to the air surrounding the cell pack. We developed the computational model to explain and separate the effects of thermal decomposition, heater, and heat loss. Thermal decomposition is intrinsic to the specific chemistry of the battery under study and also depends of the design of the materials used to build the cell. The heater was supposed to simulate a failure mode, but its

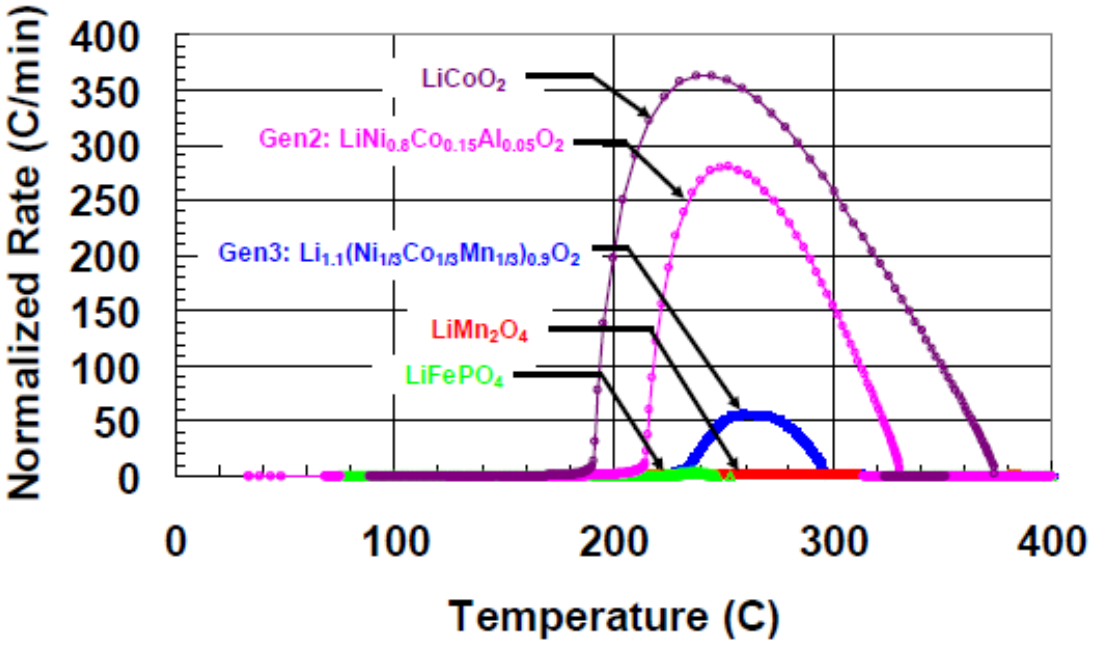

Figure 19. Accelerating rate calorimetry measurements of self-heating rates for 18650 lithium-ion batteries. Figure and data taken from [67].

effect was expected to occur only during an initial period. We found that after the initiation period, heat released by the decomposition reactions dominate the heat released during failure. In contrast, heat loss depended on the ambient conditions, packing geometry, fluid flow of air surrounding the cells, and depended on how cells were connected to one another.

To form the model, we solved the Navier-Stokes and energy equations given as follows. For the gas phase:

$$\frac{\partial \rho}{\partial t} + \nabla . \rho u = 0 \tag{14}$$

$$\rho \frac{\partial \mathrm{u}}{\partial \mathrm{t}} + \rho(u . \nabla)u = -\nabla P + \nabla . \mu \nabla u + \rho g \tag{15}$$

$$\rho C_p \frac{\partial T}{\partial t} + \rho C_p \mathrm{u} . \nabla T = \nabla . \lambda \nabla T \tag{16}$$

$$\rho = P M_w / RT \tag{17}$$

And for the solid phase:

$$\rho_s C_{ps} \frac{\partial T_s}{\partial t} = \nabla . \lambda_s \nabla T_s + Q_{ext} + Q_{r1} + Q_{r2} + Q_{r3} \tag{18}$$

Here, u, T, ρ, C_p, λ, P, M_w, R, g, and t are the velocity, temperature, density, specific heat, thermal conductivity, pressure, molecular weight of air, universal gas constant, acceleration due

to gravity, and time, respectively. The subscript *s* refers to solid phase properties. Q_{ext} is the external heat input into the heater cell for a set time period (the time until the point of thermal runaway). The heater is cylindrical, 5 mm in diameter and about 6.5 cm long. The heat input was constant in our experiments. Equations 14 to 18 were solved using COMSOL commercial software (COMSOL, Inc., Burlington, MA) on a personal computer.

Determining heat generation rates, or source terms Q_{r1} through Q_{r3} in Equation 18, was a critical part of the model. The source terms Q_{r1} through Q_{r3} were specific to the chemistry of the given active cell. They represent heat generation rates due to thermal decomposition and internal combustion of all of the components contained in the active cell. The chemical kinetics of some of the components in a cell, such as the separator and electrolyte, have been studied experimentally in isolation to determine the Arrhenius parameters. The kinetics of the entire cell is generally unknown and is not well understood. In this work, we obtained the source terms by fitting polynomial expressions to calorimetric experimental data of temperature rise rates (self-heating rates) as a function of local temperature as described below.

Sandia National Laboratory [66-68] conducted Accelerating Rate Calorimetry (ARC) measurements on the fundamental characteristics of the entire system of interest: a full, active lithium-ion battery. Their measurements showed self-heating rates (temperature rise rate) due to decomposition/combustion of an 18650 $LiCoO_2$ battery placed inside a bomb under adiabatic conditions. The exact details of their experiments are not available; however, ARC measurements typically follow a standard procedure as described elsewhere. The bomb was likely a metal vessel that was completely closed to the outside environment. During the experiment, the bomb was heated very slowly at 0.02°C/min over the course of a few days. The heating followed a typical pattern of rise and hold so that uniform temperature inside the bomb contents was achieved at all times during the holding period. As the entire battery was slowly heated beyond 100°C, exothermic decomposition reactions began to accelerate. They resulted in a significant increase in the rate of temperature rise with time as shown by the curves in Figure 19. When the temperature increased to 184°C, explosive decomposition and combustion inside the cell began causing rapid increase in the self-heating rates. During this time, the cell ruptured venting gases and liquid into the bomb causing rapid pressure rise. However, all the vented material was still contained inside the bomb vessel. As the temperature increased further, the decomposition and combustion of the bomb contents continued, and self-heating rates also continued to increase. The temperature then rose to 240°C. As the reactions progressed, the reactants were completely consumed. Despite the increasing temperature, reaction rates began to decrease due to decreasing concentrations of reactants and by dilution of the newly-formed products. This resulted in a decrease in the self-heating rates as shown in Figure 19. Finally, when all of the reactants were consumed, the temperature reached a maximum of 373°C and the self-heating rates fell to near zero.

The adiabatic temperature profile shown in Figure 19 was unique to the 18650 $LiCoO_2$ battery as long as the cell remained a closed system. In an actual application, cells lose heat to the ambient

environment and to expelled materials during rupture and venting. Therefore, Figure 19 can be used to calculate heat release rates Q_{r1} through Q_{r3} in an actual application as long as the cell remained a closed system; i.e., until the point of rupture. The ARC data was for the entire cell where the initial mass of reactants was identical to that in real applications of a single cell. Therefore, the adiabatic data shown in Figure 19 could be applied in an empirical treatment of the active cell in our model. We converted the self-heating rates shown in Figure 19 to heat generation rates by multiplying the ordinate with the density and specific heat of an active 18650 $LiCoO_2$ battery. The density remained constant during the decomposition of cell contents because the measurements were made in a closed bomb. However, the specific heat changed because of the decomposition and was therefore unknown. In this work, we assumed that specific heat was unchanged from that of the virgin cell. We fit three polynomial functions to the data shown in Figure 19, and these expressions are shown in Equations 19-21:

$$Q_r1 = 900 \cdot 2700 \cdot (360/60) \cdot (160.63 \cdot ((((T[K] - 373.15)) \,/\, 273)\text{^}6\,) - 74.252 \cdot ((((T[K] - 373.15)) \,/\, 273)\text{^}5\,) + 10.134 \cdot ((((T[K] - 373.15)) \,/\, 273)\text{^}4\,) - 0.6812 \cdot ((((T[K] - 373.15)) \,/\, 273)\text{^}3\,) + 0.0974 \cdot ((((T[K] - 373.15)) \,/\, 273)\text{^}2\,) - 0.0038 \cdot (((T[K] - 373.15)) \,/\, 273) + 6x\ 〚10〛\ \text{^}(-11)\,)$$

for 373.15 < T[K] < 457.21 and t < 1280 (19)

$$Q_r2 = 900 \cdot 2700 \cdot (360/60) \cdot (-23.614 \cdot ((((T[K] - 373.15)) \,/\, 273)\text{^}2\,) + 24.379 \cdot (((T[K] - 373.15)) \,/\, 273) - 5.2676)$$

for 457.21 < T[K] < 513.15 and t < 1280 (20)

$$Q_r3 = 900 \cdot 2700 \cdot (360/60) \cdot (1.4028 \cdot ((((T[K] - 373.15)) \,/\, 273)\text{^}3\,) - 5.8501 \cdot ((((T[K] - 373.15)) \,/\, 273)\text{^}2\,) + 4.314 \cdot (((T[K] - 373.15)) \,/\, 273) + 0.1562)$$

for 513.15 < T[K] < 646.15 and t < 1320 (21)

Substituting Equations 19-21 into Equation 18 and solving enabled description of the effects of external heating, heat loss to the ambient environment, and thermal runaway for the conditions employed in our experiments. This empirical approach gave heat release rates, but did not give reaction rates or the chemical kinetics. It should be noted that there is a need for fundamental kinetic data both on individual components of a cell as well as the entire cell so that the empirical treatment based on ARC data can be replaced with a more general approach. A more fundamental approach will account for an open and dynamic system like that of a cell during rupture and venting, and during subsequent chemical reactions in vented material outside of the cell.

The ARC data in Figure 19 also showed $LiCoO_2$ heat release rates compared to some other common lithium-ion battery chemistries. The data showed that self-heating rates for a full cell

were significantly higher than the individual components (anode, cathode, and electrolyte). Additionally, ARC measurements of Sanyo cells showed that the self-heating rates were more severe for higher SOCs. Increasing the battery voltage from 3.2 V to 4.3 V increased the self-heating rate from 500 to 1000°C/min. E. P. Roth et al. performed detailed ARC measurements and showed that anode reactions are the primary source of hydrogen generation, and the main products of decomposition are CO_2, CO, C_2H_4, and H_2 [69]. Separator decomposition began above 50°C, causing exothermic reduction of electrolyte at the electrodes. Rates of gas generation increased above 125°C with the main contribution coming from the decomposition of electrolyte. Explosive decomposition occurred between 200-250°C. The expelled material was flammable and could be ignited by a spark.

When the heater was turned on in our previous experiments, the temperature rose with time, followed by a slowing down of the temperature rise. A small jump in temperature was then observed before the cell cooled off to ambient temperature as the heater was turned off. The relative contributions to this temperature profile from the heater, the chemistry in the active cell, and venting of material from the active cell are unclear. Therefore, we considered a simple case to develop qualitative understanding. We recognized that the main role of surrogate cells was to enhance the heat loss from active and heater cells to the surrounding air. As a result, the essential components in the setup were the heater cell, active cell, and the surrounding air. Therefore, we first considered a two dimensional case where we neglected the surrogate cells and just considered two heater cells placed adjacent to an active cell as shown in Figure 20 (only half of the domain is shown due to symmetry). The finite element grid is also shown. This also allowed us to qualitatively understand the temperature rise profile seen in our experimental data and to validate the natural convective air flow. To model the buoyancy flow in surrounding air, all of the cells were placed in a relatively large rectangular box. It was known that the buoyancy flow extended to much larger distances than the cell geometry itself.

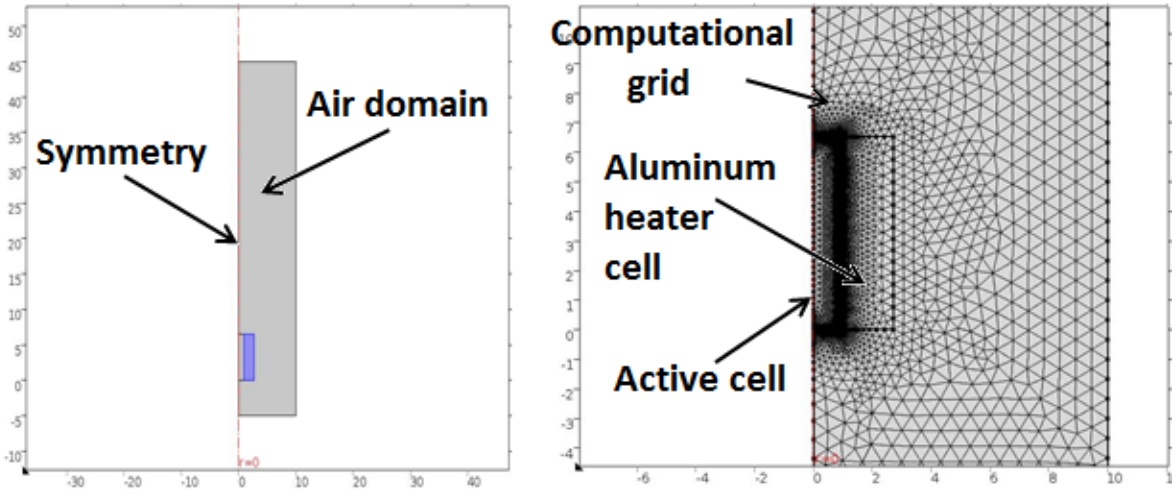

Figure 20. Graphical rendering of two dimensional model for failure tests of lithium-ion batteries.

The two dimensional model was used to establish our approach and methodology of using the ARC data. It was also used to determine the computational grid and how large a box is needed for accurate prediction of the natural convection. In the model, the heater cell was made of aluminum and the active cell had much lower thermal conductivity (0.3 W/m-K). Equations 14-18 were solved as a conjugate boundary value problem. At the solid surface, no-slip and continuity of temperature and heat flux were used to predict the surface temperature. The bottom and right of the domain were set as open boundaries and top was set as outflow. The gas and solid phase equations were coupled with the boundary conditions at the solid surface.

Figure 21 (left side) shows the velocity and temperature contours soon after the heater was turned on and heat was transferred from the heater cell to the active cell. The right half of Figure 21 shows the contours after the decomposition began but before the explosive decomposition occurred at temperatures > 463 K. Figure 21 also shows that the hot air transported heat vertically very quickly. The velocity and thermal profiles and the boundary layers developed fairly rapidly within seconds, but the magnitudes increased slowly with time. The air velocity and temperatures (both inside and outside the solid geometry) changed with time. This can be important in a large battery pack where the cells are typically packed both vertically and horizontally, and hot air can spread heat from the cell undergoing failure to the cells above. Additionally, Figure 21 shows that the air near the top of the cell was hot and could ignite flammable gases ejected due to rupture of the cell.

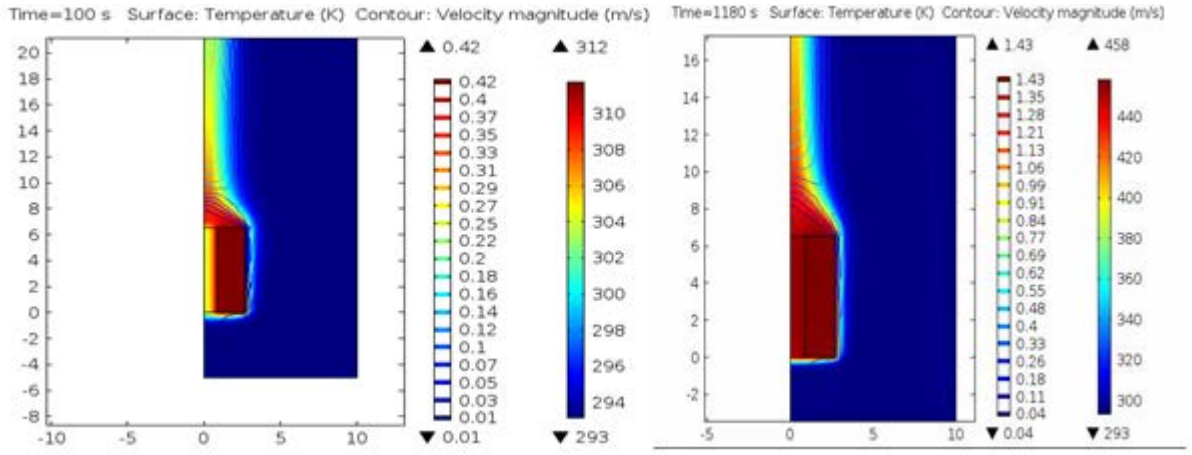

Figure 21. Velocity and temperature contours at 100s (left plot) and 1180s (right plot) obtained from the two dimensional model.

Figure 22 shows how the temperature at the contact point between heater and active cells changed with time. The heater was turned on at time zero and tuned off after 22 minutes. The profiles were qualitatively very similar to those displayed in our previous experimental work [26]. The profiles in Figure 22 show that the external heater, rather than the chemical heat (Q_{r1}) released from the cell internals, dominated the initial time period up until the temperature reached 184°C. Once the temperature reached 184°C, Q_{r2} and Q_{r3}, which represent the explosive and chemical heat release rates, dominated the temperature rise. The model showed that the

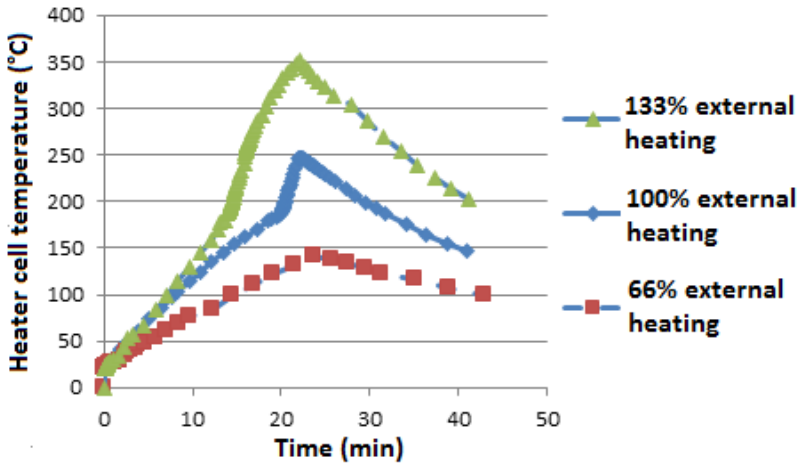

Figure 22. Evolution of temperature at the heater-active cell junction for different external heating rates. The heater was turned on for a duration of 22 minutes in all cases.

temperature profile peak, which was also observed in the experimental data, was actually due to the exothermic decomposition/ combustion reactions. The profile leading up to the temperature peak was influenced mainly by the external heating.

Figure 23 shows the heat flux from the heater cell to the active cell. Initially, it was positive when the heater was turned on and all the cells were at ambient conditions. The heat flux then went to zero as the active cell temperature started to rise due to the decomposition reactions. As the active cell temperature rose rapidly due to rapid chemical heat generation, the heat was transferred from the active cell to the heater cell as indicated by the negative flux. When the chemical reactions were completed, the heat was dissipated, and the heat flux dropped back to near zero.

To take our modeling efforts further, we developed a three dimensional version of the model described above using the COMSOL platform. Figure 24 shows a nine-cell geometry (only half of the domain is again shown due to symmetry) along with air gaps between cells. The experiments were conducted with both hexagonal and rectangular arrangements along with the finite element grid. The model can be easily manipulated to incorporate either configuration.

Figure 25 shows that the solid geometry was placed inside a large (20 cm radius and 40 cm long) cylinder, as was done in the two dimensional version of the model that included a large box. Thus, the actual three dimensional computational domain extended many times the volume of the solid structure to capture the three dimensional buoyancy flow.

Figure 26 shows that the air above the solid geometry became significantly hot (> 500 K), which was close to the ignition temperature of hydrocarbon gases. The hot

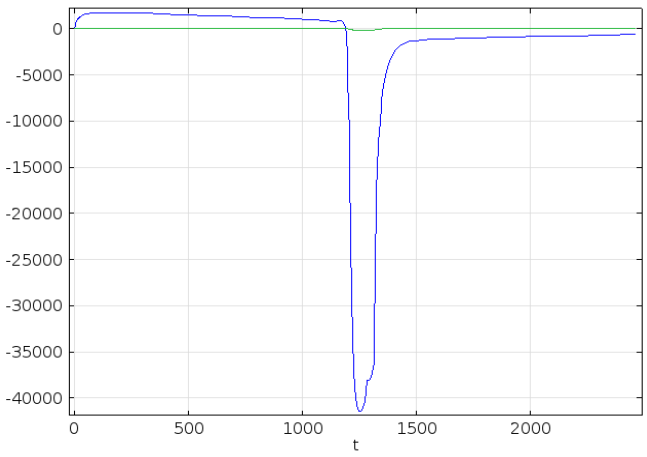

Figure 23. Heat flux at the junction between heater and active cells.

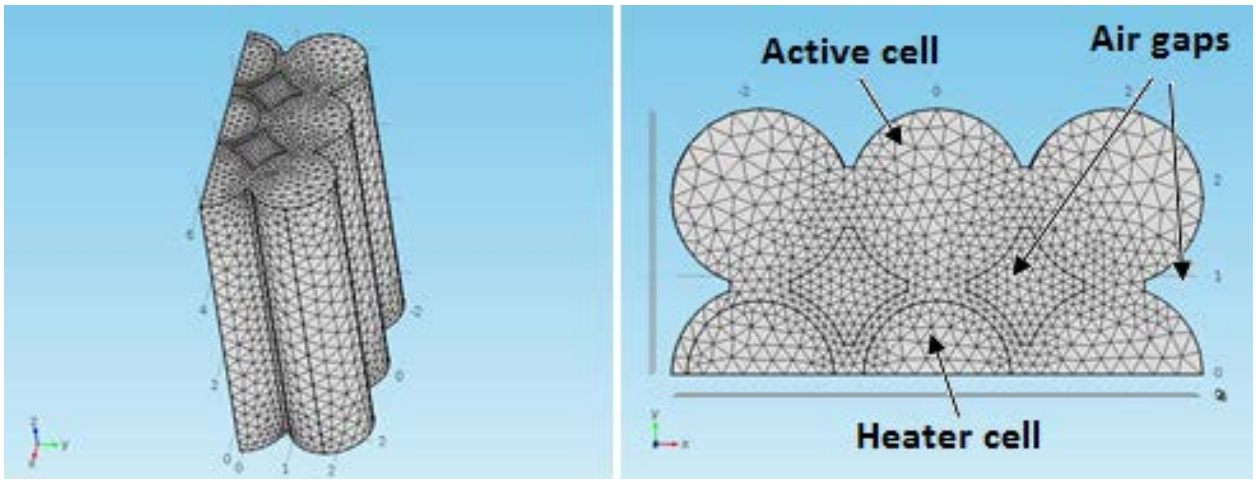

Figure 24. Three dimensional model geometry (only half of the domain is shown due to symmetry) consisting of one active cell, one heater cell, and seven surrogate cells, along with the computational grid.

region extended to twice the height of the solid geometry. The temperature of the active cell reached 627 K after 1225 seconds.

Figure 27 shows the velocity and temperature contours for the three dimensional model at 1300 seconds. The velocity contours are shown on a plane cut across the middle of the cell structure. The active cell was relatively hotter than the rest of the cells, reaching a maximum temperature of 631 K. The hot air flowed out from the top of the large enclosure which was about 30 cm away from the cells. The velocity reached 0.83 m/s.

Figure 28 compares the three dimensional and two dimensional model predictions with the experimental data for temperature rise at the junction between the active and heater cells as shown in Figure 24. Given that we used an empirical technique to determine the heat generation

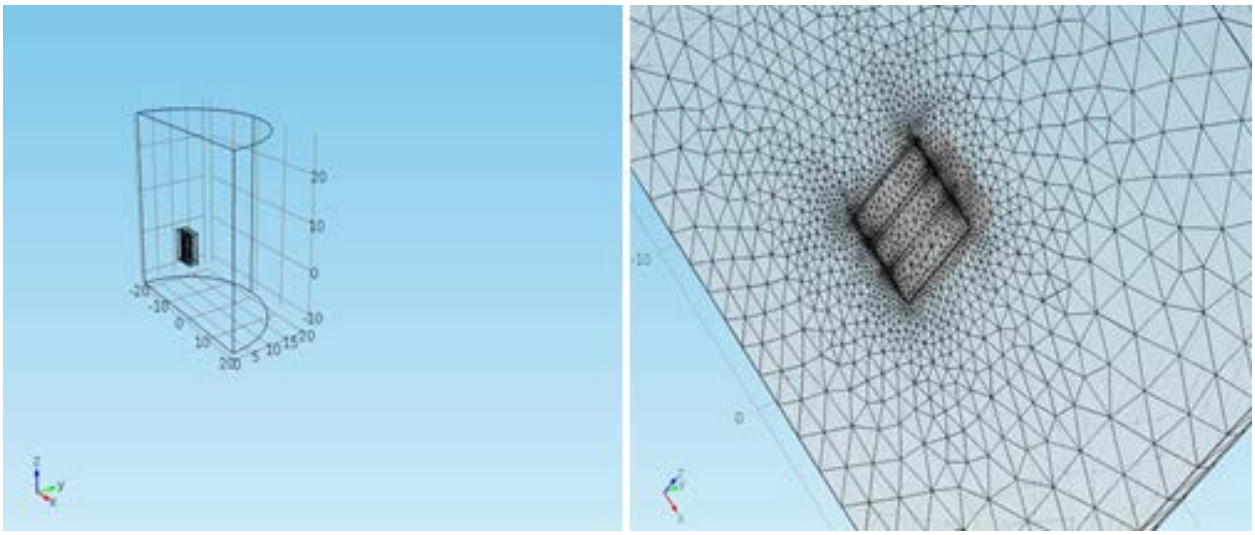

Figure 25. Computational domain and surface grid for three dimensional model near the solid geometry.

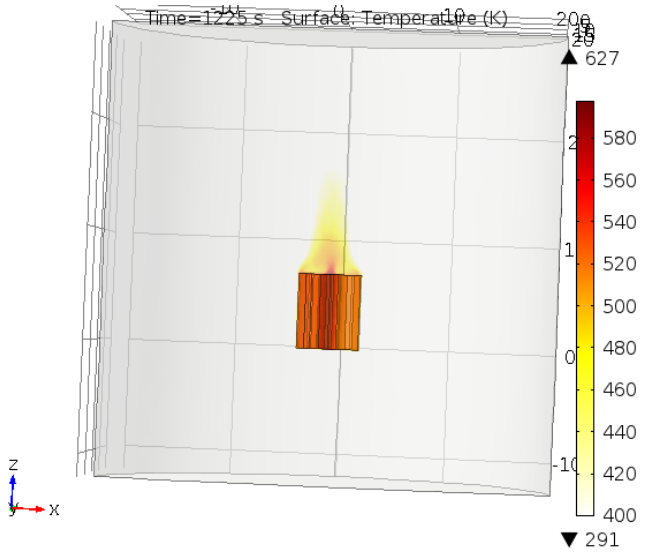

Figure 26. Three dimensional model predictions of thermal contours in solid and gas phases as t=1225s.

rates because very little is understood about the chemistry of active cell contents, it is surprising that the model predictions were in reasonable agreement with the experimental data. However, there were a few significant differences between the three dimensional model results and the experimental data. First, the temperature rise during the first three minutes (up to 150°C) was much faster in the experiments compared to the model prediction. After the first four minutes, however, the temperature rise slopes were comparable between the model and experimental data. Second, the onset temperature for the explosive decomposition (Q_{r2}) was higher (238°C) compared to that for the model (184°C). This is because the ARC data shown in Figure 19 exhibited a lower onset temperature than was observed in our experiments.

A clear understanding of the differences between the experiments and models would require measurements of chemical kinetics and how they are affected by SOC. For example, the active cell used in our experiments was overcharged, while the active cell used in ARC measurements was not overcharged. In our models, we neglected the effect of SOC on heat generation rates. This may suggest that SOC had a significant effect on temperature rise during the first three minutes when the temperature rose to 150°C. However, it is less clear how SOC could increase the onset temperature for explosive decomposition (Q_{r2}) by 54°C. Indeed, ARC experiments conducted by E. P Roth and D. H. Doughty showed SOC effects at temperatures below 150°C [69]. They also showed that increased SOC decreased the onset temperature. To understand this, we intend to perform experiments and modeling for the case where the active cell is

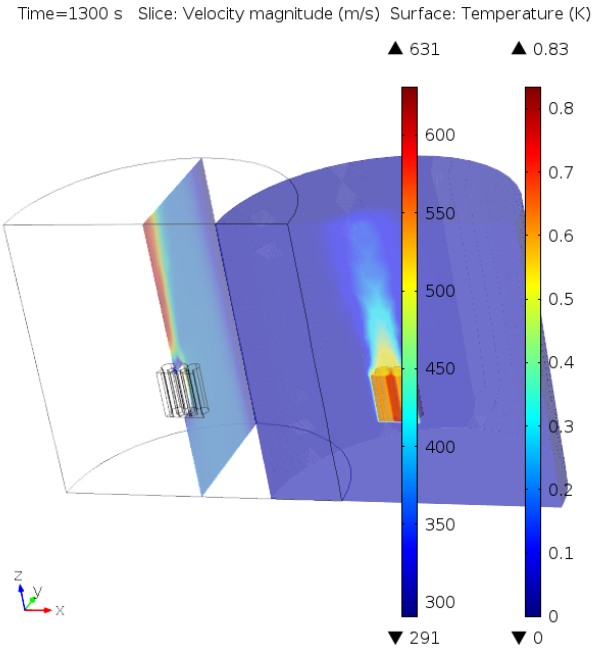

Figure 27. Three dimensional model predictions for buoyancy-driven flow of air and temperature contours at t=1300s.

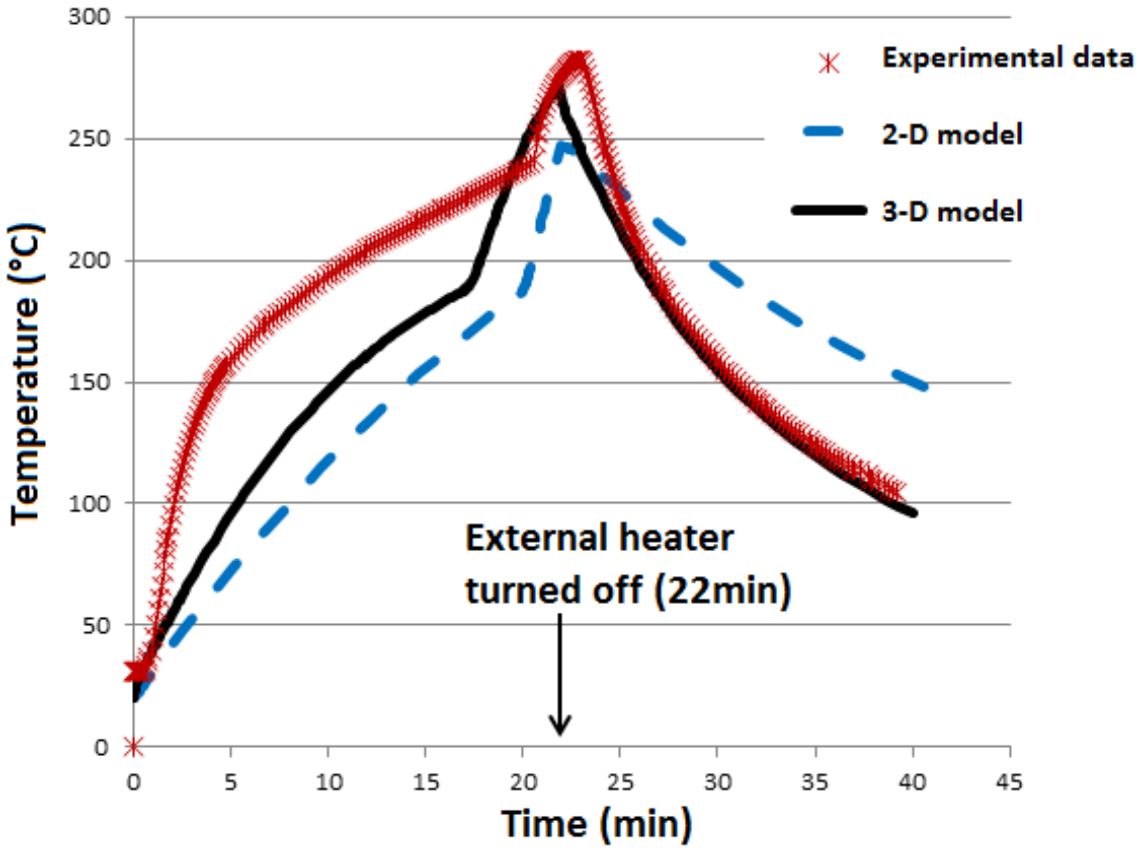

Figure 28. Comparison of model predictions with experimental data for surface temperatures near the contact region between active and heater cells.

uncharged and compare with data of the overcharged cell. We have also begun to further characterize our external heater because it seemed to have a significant effect on the temperature rise during the first 18 minutes. This was done by measuring surface temperature rise with time for the bare heater placed directly in ambient air, or by placing the heater cell in ambient air. These can be modeled as a special case of Equations 14-18 and compared with experimental data.

4.0 Summary & Conclusions

We have examined in greater detail the thermal and electrochemical behavior of lithium-ion batteries prior to and during failure and the associated thermal propagation. This effort has included the development of thermally-similar surrogate cells to mimic the thermal diffusivity of active cells, the measurement of heat capacity and conductivity of active cells, the calculation of the heat release rate of active cells during thermal abuse, and the incorporation of these data into a computational model developed to simulate failure of individual and multi-cell packs. We have also established an experimental, non-invasive method to measure the internal cell

temperature using EIS. These methods allow the application of validated computational thermal models that temporally and spatially resolve heat transfer, prior to and during failure, and the associated measurement of the cell temperature.

The surrogate cell design replicated the thermal diffusivity while capturing the anisotropic thermal conductivity of active cells. Thin, coiled layers, or a "jelly roll", of mica and stainless steel, placed inside an 18650 cell casing, most accurately mimicked the thermal properties of an active cell. Thermocouples were placed inside the casing to measure internal temperatures at multiple radial locations. This design provides a reusable, nonflammable surrogate cell package that will provide data during destructive tests that will indicate cell failure. Because conventional materials were used and the thermal similarity was validated experimentally and non-destructively, the design can be altered and adapted for additional cell chemistries.

We developed and compared a number of methods to extract the thermal properties of an active cell, with particular focus on the anisotropic thermal conductivity and the heat capacity. We found that assuming a lumped mass with convective heat transfer and an analytical solution to the heat equation provided a radial conductivity value within an order of magnitude of those reported in literature and heat capacity within 15%. A numerical method that fit temperature and heat flux measurements to a higher resolution than the analytical model provided values with greater confidence and more similitude to those found in literature. These data provide input into computational thermal models for the cell and battery package.

Simple Dewar calorimeter measurements provided rough heat capacity measurements at standard operating temperatures, but they were not able to provide the resolution nor the full calorimetric behavior of an active cell. In particular, these experiments did not account for the exothermicity of SEI decomposition that occurs when the metastable surface compounds decompose and expose the anode to the electrolyte that occurs during early failure at temperatures above ~80°C. Additionally, calorimetry is not applicable to active cells during the more exothermic processes of thermal runaway where rapid exothermic reactions cause internal or external combustion and cell destruction.

We developed an EIS-based, non-invasive internal temperature measurement method that can be used to instantaneously monitor individual cell temperatures. This method will extract internal cell temperatures from failure testing and provide validation data for individual cell and battery system modeling. This instrumentation method will also provide cell temperature for battery control systems and allow system designers to detect, anticipate, and mitigate battery failure.

Numerical modeling methods were developed using COMSOL software to simulate the thermal failure processes we have observed experimentally that are portable to larger battery systems. In particular, we developed a method to capture thermal runaway and the associated heat release and transfer to adjacent cells. We used ARC data and calculated heat release rate expressions that we integrated into two and three-dimensional thermal models of experiments until the point

of cell rupture. The model predictions for self-heating rates are in good agreement with the experimental measurements except for the first few minutes in a 40 minute run, possibly due to the effects of overcharge. The results show that ARC can provide valuable information from which fundamental chemical kinetics models could be constructed to predict thermal runaway with venting of gases beyond the point of cell rupture. Finally, future modeling work will be performed using the ANSYS/FLUENT software platform, and we will also collaborate closely with Dr. Robert Kee at the Colorado School of Mines, who has developed thermal and electrochemical packages using the ANSYS/FLUENT program. Experimental data and modeling work will be exchanged with Dr. Kee to leverage the expertise of both parties and produce more accurate models of lithium-ion behavior before, during and after failure.

5.0 References

1. <http://www.theinquirer.net/inquirer/news/1042700/dell-laptop-explodes-japanese-conference>

2. <http://www.foxnews.com/leisure/2011/11/25/new-post-accident-chevy-volt-engine-fires-prompt-investigation/>

3. <http://worldnews.nbcnews.com/_news/2013/07/12/19438748-boeing-787-dreamliner-catches-fire-at-london-heathrow-airport>

4. <http://www.dailytech.com/Two+More+Boeing+787+Dreamliners+Catch+Fire+Suffer+Technical+Issues/article31962.htm>

5. D. R. Pendergast, E. P. DeMauro, M. Fletcher, E. Stimson and J. C. Mollendorf, "A rechargeable lithium-ion battery module for underwater use." *J. Power Sources* **196** (2011) 793-800.

6. C. Winchester and D. Kiernan, "Lithium Battery Safety: Good Batteries Gone Bad." A joint service presentation and discussion, US Army CECOM, Joint Service Power Expo, 5 May 2005.

7. J. Dow and C. Batchelor, "Navy Lithium Battery Safety." Department of Defense Explosive Safety Board 34th Seminar, Portland, Oregon, ADM002313, 14 July 2010.

8. G. J. Govar and J. A. Banner, "Safety testing of lithium ion batteries for Navy devices." *IEEE AESS Systems Magazine* **18** (2003) 17-20.

9. S. Tippmann, D. Walper, L. Balboa, B. Spier and W. G. Bessler, "Low-temperature charging of lithium-ion cells part 1: Electrochemical modeling and experimental investigation of degradation behavior." *J. Power Sources* **252** (2014) 305-316.

10. M. Keyser, K. Smith, A. Pesaran, J. Ireland, G. Kim, K. Long and J. Neubauer, "Battery Thermal Modeling and Testing." *U.S. DOE Hydrogen Program and Vehicle Technologies Program Annual Merit Review & Peer Evaluation Meeting*, 9-13 May 2011, Arlington, Virginia.

11. B. Wu, V. Yufit, M. Marinescu, G. J. Offer, R. F. Martinez-Botas and N. P. Brandon, "Coupled thermal-electrochemical modelling of uneven heat generation in lithium-ion battery packs." *J. Power Sources* **243** (2013) 544-554.

12. A. Ahmad, A. Pesaran, G.-H. Kim, K. Smith, S. Santhanagopalan and K.-J. Lee, "Overview of computer-aided engineering of batteries and introduction to multi-scale, multi-dimensional modeling of Li-ion batteries." *U.S. DOE Hydrogen Program and Vehicle Technologies Program Annual Merit Review & Peer Evaluation Meeting*, 14-18 May 2012, Arlington, Virginia.

13. T. A. Haupt, G. Henley, B. S. Parihar, R. Kirkland, J. Floyd, J. Scheffey, P. A. Tatem and F. W. Williams, "User manual for graphical user interface version 2.10 with fire and smoke simulation model (FSSIM) version 1.2." *NRL Memorandum Report* NRL/MR/6180-10-9244, 10 May 2010.

14. J. E. Floyd, S. P. Hunt and F. W. Williams, "Fire and smoke simulator (FSSIM) version 1.7." *NRL Letter Report* 6104/0003, 02 April 2012.

15. ASAP: Advanced Survivability Assessment Program, Naval Surface Warfare Center, Carderock Division, Bethesda, MD.

16. X. Lin, H. E. Perez, S. Mohan, J. B. Siegel, A. G. Stefanopoulou, Y. Deng and M. P. Castanier, "A lumped-parameter electro-thermal model for cylindrical batteries." *J. Power Sources* **257** (2014) 1-11.

17. C. Forgez, D. V. Do, G. Friedrich, M. Morcrette and C. Delacourt, "Thermal modeling of a cylindrical $LiFePO_4$/graphite lithium-ion battery." *J. Power Sources* **195** (2010) 2961-2968.

18. T. B. Bandhauer, S. Garimella and T. F. Fuller, "A critical review of thermal issues in lithium-ion batteries." *J. Electrochem. Soc.* **158** (2011) R1-R25.

19. D. Belov and M.-H. Yang, "Investigation of the kinetic mechanism in overcharge process for Li-ion battery." *Solid State Ionics* **179** (2008) 1816-1821.

20. F. W. Williams, H. V. Pham, A. F. Durkin and B. D. Gould, "The heat Release rate from lithium polymer and lithium-iron phosphate batteries thermally stressed." *NRL Letter Report* 6104/0006, 28 April 2010.

21. G. G. Back, J. Williamson and F. W. Williams, “Lithium battery casualty mitigation system (LBCMS) development – potential gas production caused by electrolysis.” *NRL Letter Report* 6104/0015, 09 July 2010.

22. F. W. Williams, A. F. Durkin, C. S. Winchester and H. V. Pham, “Tests to support development of a lithium battery casualty mitigation system (LBCMS) - phase 1: heat release rate baseline data.” *NRL Letter Report* 6104/0017, 13 September 2010.

23. G. G. Back, A. F. Durkin, X. Nguyen, H. V. Pham, S. Duncan, C. S. Winchester, J. Gratz and F. W. Williams, “Lithium battery casualty mitigation system (LBCMS) development tests – brass board tests (quick look).” *NRL Letter Report* 6104/0009, 05 July 2011.

24. F. W. Williams, H. V. Pham, A. F. Durkin, C. S. Winchester and G. G. Back, “Lithium battery casualty mitigation system (LBCMS) – brass board test results.” *NRL Letter Report* 6104/0015, 14 November 2011.

25. F. W. Williams and S. L. Rose-Pehrsson, “A test plan for the tips program to measure the gaseous species production of generic lithium batteries exposed to thermal abuse.” *NRL Letter Report* 6104/0005, 19 April 2010.

26. C. R. Field, M. H. Hammond, S. G. Tuttle, B. A. Williams, S. L. Rose-Pehrsson, N. S. Spinner, K. M. Myers and A. L. Lubrano, “Demonstration of experimental infrastructure for studying cell-to-cell failure propagation in lithium-ion batteries.” *NRL Memorandum Report* NRL/MR/6180-14-9563, 11 September 2014.

27. S. J. Drake, D. A. Wetz, J. K. Ostanek, S. P. Miller, J. M. Heinzel and A. Jain, "Measurement of anisotropic thermophysical properties of cylindrical Li-ion cells." *J. Power Sources* **252** (2014) 298-304.

28. G. Zhang, L. Cao, S. Ge, C.-Y. Wang, C. E. Shaffer and C. D. Rahn, “In situ measurement of radial temperature distributions in cylindrical Li-ion cells.” *J. Electrochem. Soc.* **161** (2014) A1499-A1507.

29. D. W. Green and R. H. Perry, "Perry's Chemical Engineers' Handbook, 8th Edition." New York: McGraw-Hill (2008).

30. Metallic Materials Properties Development and Standardization (MMPDS-07). Battelle Memorial Institute (2012).

31. R. B. Bird, W. E. Stewart and E. N. Lightfoot, "Transport Phenomena, Second Edition." India: John Wiley & Sons (2005).

32. T. Hirono and W. Tanikawa, "Implications of the thermal properties and kinetic parameters of dehydroxylation of mica minerals for fault weakening, frictional heating, and earthquake energetics." *Earth Planet. Sci. Lett.* **307** (2011) 161-172.

33. L. P. Ogorodova, I. A. Kiseleva, L. V. Mel'chakova and T. N. Shuriga, "The thermodynamic characteristics of natural iron-lithium micas." *Russ. J. Phys. Chem. A* **82** (2008) 942-945.

34. A. S. Gray and C. Uher, "Thermal conductivity of mica at low temperatures." *J. Mater. Sci.* **12** (1977) 959-965.

35. H. Maleki, S. Al Hallaj, J. R. Selman, R. B. Dinwiddie and H. Wang, "Thermal properties of lithium-ion battery and components." *J. Electrochem. Soc.* **146** (1999) 947-954.

36. E. Barsoukov, J. H. Jang and H. Lee, "Thermal impedance spectroscopy for Li-ion batteries using heat-pulse response analysis." *J. Power Sources* **109** (2002) 313-320.

37. A. A. Pesaran and M. Keyser, "Thermal characteristics of selected EV and HEV batteries." *Annual Battery Conference: Advances and Applications,* Long Beach, CA, 9-12 January 2001.

38. S.-C. Chen, Y.-Y. Wang and C.-C. Wan, "Thermal analysis of spirally wound lithium batteries." *J. Electrochem. Soc.* **153** (2006) A637-A648.

39. N. S. Spinner, S. G. Tuttle and S. L. Rose-Pehrsson, "Novel 18650 surrogate cell design with anisotropic thermal properties." Manuscript in preparation.

40. R. W. Serth and T. G. Lestina, "Process Heat Transfer: Principles, Applications and Rules of Thumb." Oxford, UK: Elsevier (2014).

41. J. Blumm, A. Lindemann, M. Meyer and C. Strasser, "Characterization of PTFE using advanced thermal analysis techniques." *Int. J. Thermophys.* **31** (2010) 1919-1927.

42. G. T. Furukawa, R. E. McCoskey and G. J. King, "Calorimetric properties of polytetrafluoroethylene (Teflon) from 0° to 365° K." *J. Res. Natl. Bur. Stand.* **49** (1952) 273-278.

43. D. M. Price and M. Jarratt, "Thermal conductivity of PTFE and PTFE composites." *Thermochim. Acta* **392-393** (2002) 231-236.

44. M. Baginska, B. J. Blaiszik, R. J. Merriman, N. R. Sottos, J. S. Moore and S. R. White, "Autonomic shutdown of lithium-ion batteries using thermoresponsive microspheres." *Adv. Energy Mater.* **2** (2012) 583-590.

45. N. S. Spinner, R. Mazurick, A. Brandon, S. G. Tuttle and S. L. Rose-Pehrsson, "Experimental, numerical and analytical determination of thermophysical properties of commercial 18650 $LiCoO_2$ lithium-ion battery." Manuscript in preparation.

46. F. Larsson and B.-E. Mellander, “Abuse by external heating, overcharge and short circuiting of commercial lithium-ion battery cells.” *J. Electrochem. Soc.* **161** (2014) A1611-A1617.

47. P. G. Balakrishnan, R. Ramesh and T. Prem Kumar, “Safety mechanisms in lithium-ion batteries.” *J. Power Sources* **155** (2006) 401-414.

48. R. Srinivasan, B. G. Carkhuff, M. H. Butler and A. C. Baisden, “Instantaneous measurement of the internal temperature in lithium-ion rechargeable cells.” *Electrochim. Acta* **56** (2011) 6198-6204.

49. P. Suresh, A. K. Shukla and N. Munichandraiah, “Temperature dependence studies of a.c. impedance of lithium-ion cells.” *J. Appl. Electrochem.* **32** (2002) 267-273.

50. S. S. Zhang, K. Xu and T. R. Jow, “Electrochemical impedance study on the low temperature of Li-ion batteries.” *Electrochim. Acta* **49** (2004) 1057-1061.

51. G. Nagasubramanian, “Electrical characteristics of 18650 Li-ion cells at low temperatures.” *J. Appl. Electrochem.* **31** (2001) 99-104.

52. R. Srinivasan and B. G. Carkhuff, “Empirical analysis of contributing factors to heating in lithium-ion cells: Anode entropy versus internal resistance.” *J. Power Sources* **241** (2013) 560-566.

53. J. P. Schmidt, S. Arnold, A. Loges, D. Werner, T. Wetzel and E. Ivers-Tiffée, “Measurement of the internal cell temperature via impedance: Evaluation and application of a new method.” *J. Power Sources* **243** (2013) 110-117.

54. J. P. Schmidt, D. Manka, D. Klotz and E. Ivers-Tiffée, “Investigation of the thermal properties of a Li-ion pouch-cell by electrothermal impedance spectroscopy.” *J. Power Sources* **196** (2011) 8140-8146.

55. C. T. Love, M. B. V. Virji, R. E. Rocheleau and K. E. Swider-Lyons, “State-of-health monitoring of 18650 4S packs with a single-point impedance diagnostic.” *J. Power Sources* **266** (2014) 512-519.

56. C. T. Love and K. Swider-Lyons, “Impedance diagnostic for overcharged lithium-ion batteries.” *Electrochem. Solid-State Lett.* **15** (2012) A53-A56.

57. L. H. J. Raijmakers, D. L. Danilov, J. P. M. van Lammeren, M. J. G. Lammers and P. H. L. Notten, “Sensorless battery temperature measurements based on electrochemical impedance spectroscopy.” *J. Power Sources* **247** (2014) 539-544.

58. M. G. S. R. Thomas, P. G. Bruce and J. B. Goodenough, "AC impedance analysis of polycrystalline insertion electrodes: application to $Li_{1-x}CoO_2$." *J. Electrochem. Soc.* **132** (1985) 1521-1528.

59. Y. Liu, Q. Liu, Z. Li, Y. Ren, J. Xie, H. He and F. Xu, "Failure study of commercial $LiFePO_4$ cells in over-discharge conditions using electrochemical impedance spectroscopy." *J. Electrochem. Soc.* **161** (2014) A620-A632.

60. M. Kassem, J. Bernard, R. Revel, S. Pélissier, F. Duclaud and C. Delacourt, "Calendar aging of a graphite/$LiFePO_4$ cell." *J. Power Sources* **208** (2012) 296-305.

61. N. S. Spinner, C. T. Love, S. G. Tuttle, K. Swider-Lyons and S. L. Rose-Pehrsson, "Non-invasive wide-range internal temperature monitoring of commercial 18650 Li-ion battery via single-frequency EIS." Manuscript in preparation.

62. G.-H. Kim, A. Pesaran and R. Spotnitz, "A three-dimensional thermal abuse model for lithium-ion cells." *J. Power Sources* **170** (2007) 476-489.

63. S. Al Hallaj, H. Maleki, J. S. Hong and J. R. Selman, "Thermal modeling and design considerations of lithium-ion batteries." *J. Power Sources* **83** (1999) 1-8.

64. D. H. Jeon, "Numerical modeling of lithium ion battery for predicting thermal behavior in a cylindrical cell." *Curr. Appl. Phys.* **14** (2014) 196-205.

65. A. A. Pesaran, G.-H. Kim, K. Smith and E. C. Darcy, "Designing Safe Lithium-Ion Battery Packs Using Thermal Abuse Models." NREL/PR-540-45388, 4th International Conference on Lithium Mobile Power, Las Vegas, NV, 8-9 December 2008.

66. D. H. Doughty and A. A. Pesaran, "Vehicle Battery Safety Roadmap Guidance." National Renewable Energy Laboratory, Golden, CO, NREL/SR-5400-54404, October 2012.

67. D. Doughty and E. P. Roth, "A General Discussion of Li Ion Battery Safety." Electrochemical Society, Interface, Summer 2012.

68. E. P Roth, C. C. Crafts, D. H. Doughty and J. McBreen, "Advanced Technology Development Program for Lithium-Ion Batteries: Thermal Abuse Performance of 18650 Li-Ion Cells." Sandia National Laboratory, Albuquerque, NM, SAND2004—0584, March 2004.

69. E. P. Roth and D. H. Doughty, "Thermal abuse performance of high-power 18650 Li-ion cells." *J. Power Sources* **128** (2004) 308-318.